


Vacuum-induced quantum-beat-enabled photon antibunchingZhiming Wu,^{*} Jiahua Li^{✉,†} and Ying Wu[‡]*School of Physics, Huazhong University of Science and Technology, Wuhan 430074, People's Republic of China* (Received 28 April 2023; revised 14 July 2023; accepted 10 August 2023; published 25 August 2023)

Vacuum-induced coupling (VIC), arising from the quantum interference between the spontaneous emission pathways from the excited doublet to a common ground state, has attracted significant research interest and has been observed in recent experiments. Here, we present an alternative route to probe the existence of VIC by means of the coherence statistics of photon antibunching and show that, under realistic experimental conditions, the vacuum-induced quantum beat (VIQB) can enable strong photon antibunching with high brightness in an optical nanofiber (ONF) cavity quantum electrodynamics (CQED) system. We find that the occurrence of the photon antibunching corresponds to the existence of the VIC, indicating that the photon antibunching can be an important witness for VIC. In addition, a strong photon antibunching effect appears in the weak-coupling regime of light-atom interactions when the VIQB is present, as a result of the destructive quantum interference between the different paths for two-photon excitation. Furthermore, we find that strong photon antibunching can be generated within a certain driving frequency range in the present system, which can relax the requirement for the driving frequency in the ONF CQED system. Also, we compare the analytical and numerical results of the second-order intensity correlation function, and they are in good agreement. The present study builds a bridge between the photon antibunching and the VIC and VIQB, which is useful for well understanding and researching a tunable single-photon source, as well as enabling potential applications in quantum information processing and quantum communications.

DOI: [10.1103/PhysRevA.108.023727](https://doi.org/10.1103/PhysRevA.108.023727)**I. INTRODUCTION**

Quantum beat is a fundamental and important quantum phenomenon, referring to the interference effect in the radiation emitted from different excited levels in multilevel systems [1,2]. It occurs in the modulation of the decay by spontaneous emission of multilevel systems owing to the energy difference among transitions [3]. Periodic interference between different energy levels results in energy exchange and periodic modulation of the radiated field intensity [4], usually appearing in the time-resolved fluorescence [5,6], the wave mixing [7,8], or the absorption profiles [9,10]. Quantum beat is a significant tool of nonlinear spectroscopy [4,11], offering a powerful means of measuring the energy differences between excited levels in many experimental platforms, including atoms [12,13], molecules [14,15], quantum dots [16,17], semiconductors [18,19], and superconductors [20]. The study of quantum beat is important for understanding the dephasing processes and the coherent characteristics in atoms and molecules, as well as for developing quantum technologies, such as quantum sensing [20], quantum storage [21,22], and quantum gates [23,24].

In 2021, Han *et al.* observed experimentally that quantum beat can occur in a three-level atomic system initially prepared in a single excited level due to the vacuum-induced coupling

(VIC) between excited levels [4]. Recently, the VIC that arises from the quantum interference between the spontaneous emission pathways from the excited doublet to a common ground state has attracted tremendous research interest and has been experimentally observed (see, e.g., Refs. [4,25]). Alternatively, quantum beat can also be observed in photon antibunching in a three-level atomic system [26,27], yet the relationship between photon antibunching and quantum beat remains mostly unexplored. Photon antibunching refers to the statistical property of a light field that the excitation of a first photon can block the transmission of subsequent photons [28]. In recent years, significant progress has been achieved in cavity quantum electrodynamics (CQED) systems composed of an optical microcavity strongly coupled to a single atom, which can generate large optical nonlinearity even at the single-photon level [29–31] and induce an anharmonic Jaynes-Cummings ladder [32–34]. Thanks to the anharmonic energy-level spacing, the population of the two-photon state can be substantially suppressed when the nonlinear energy shift in the two-photon state is greater than the loss of the optical cavity, resulting in only one photon allowed in the coupled system [35–38]. This phenomenon is called the conventional photon blockade, in which the photons show strong antibunching [39–41]. In contrast, there is another avenue to get photon antibunching in a quantum optical system with weak nonlinearity, known as unconventional photon blockade [42–45]. This achieved photon antibunching is based on quantum destructive interference between the two or more different quantum paths from a one-photon state transiting to a two-photon state [43]. The photon antibunching effect can be

^{*}zhiming@hust.edu.cn[†]Corresponding author: huajia_li@163.com[‡]yingwu2@126.com

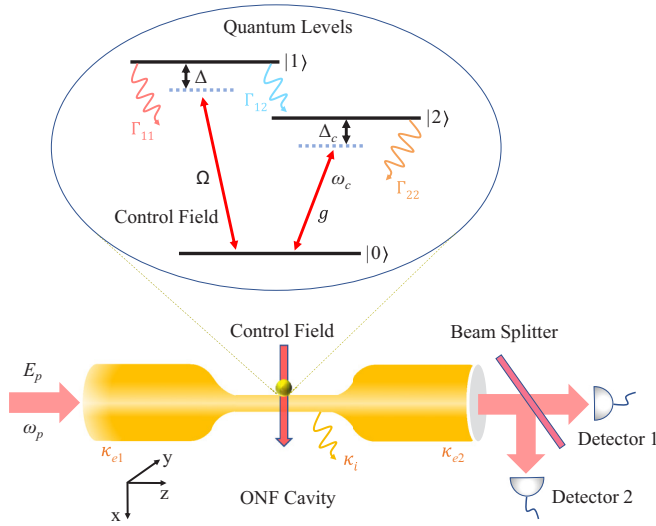


FIG. 1. Schematic representation of the ONF CQED system. The ONF CQED system consists of a single three-level V-type atom (the small gold sphere) trapped in the vicinity of a tapered ONF-based cavity. The top inset shows atomic level structure, relevant damping, and corresponding laser coupling involved in the scheme. The ground state is denoted by $|0\rangle$ and the two excited states are represented by $|1\rangle$ and $|2\rangle$. The x , y , and z axes are defined as shown in the bottom left corner. The external laser field with the central frequency ω_p and the amplitude E_p is applied to coherently drive the cavity mode with the resonance frequency ω_c and to couple the $|2\rangle \leftrightarrow |0\rangle$ excited transition via the left-hand cavity mirror along the axial (z) direction. At the same time, the free-space control laser with the central frequency ω and the Rabi frequency Ω interacts with the atom and couples the $|1\rangle \leftrightarrow |0\rangle$ excited transition from the open side of the cavity along the vertical (x) direction. The second-order intensity correlation function $g^{(2)}(0)$ of the transmitted field through the right-hand cavity mirror can be measured by using one ordinary 50:50 nonpolarizing beam splitter and two single-photon detectors. Here κ_{e1} and κ_{e2} are the damping rates of the left- and right-hand cavity mirrors, and κ_i is the inner damping rate of the cavity. The cavity is chosen to be symmetric, i.e., $\kappa_{e1} = \kappa_{e2}$. The total damping rate of the cavity is given by the sum $\kappa = \kappa_{e1} + \kappa_{e2} + \kappa_i$. Γ_{11} and Γ_{22} are the damping rates of the excited states $|1\rangle$ and $|2\rangle$ to the ground state $|0\rangle$, respectively. Γ_{12} represents the cross-damping rate between the excited states $|1\rangle$ and $|2\rangle$, namely, the VIC. Other symbols are defined in the text

implemented for a single-photon source [46–48], which plays an important role in quantum optics and quantum information technologies [49–52].

Inspired by such a three-level quantum model [4] mentioned above, here we put forward an alternative route to probe the existence of the VIC utilizing the quantum statistics of photon antibunching and further reveal that the vacuum-induced quantum beat (VIQB) can enable photon antibunching in a weak-coupling CQED architecture. Specifically, the proposed CQED system consists of a tapered optical nanofiber (ONF)-based [53–56] single-mode cavity containing a single three-level V-type atom (with two closely lying upper states $|1\rangle$ and $|2\rangle$, and one ground state $|0\rangle$); see Fig. 1 for a sketch), which is subject to a control field and is excited

by an external driving light field from the left end of the cavity. We find that the coherence statistics of photon antibunching and the quantum beat dynamics of the ONF CQED system with VIC are distinct from those without VIC. Furthermore, we find that the occurrence of photon antibunching corresponds to the existence of VIC, indicating that the photon antibunching can be an important witness for VIC and can be used to probe the existence of VIC. By means of both the master equation approach and the Schrödinger equation approach, we present detailed analytical and numerical results of the second-order intensity correlation function $g^{(2)}(0)$, in which the analytical results are in good agreement with the numerical simulations.

Alternatively, using experimentally realistic parameter values, we also investigate the influence of system parameters on the photon antibunching. By reasonably tuning the system parameters, a strong photon antibunching can occur in the weak-coupling “bad-cavity” regime of CQED when the VIQB is present, as a result of the destructive quantum interference between the different paths for the two-photon excitation, which is beneficial to the use of low-finesse cavities that are readily accessible in many CQED systems. In this case, the strong photon antibunching can be detected near the strong intensity of the emitted light from the ONF-based cavity at the same time, which provides a guiding significance for practical experimental design to a certain extent. In our proposed scheme, strong photon antibunching with large brightness can be generated within a certain driving frequency range, which can relax the requirement for the driving frequency in the ONF CQED system. Also, we demonstrate that this scheme of probing the existence of the VIC utilizing the coherence statistics of photon antibunching can be implemented based on a real physical platform. The present study builds a bridge between the photon antibunching and the VIC and VIQB. Our achievable results may be useful for building a tunable single-photon source and enabling potential applications in quantum information processing [57,58] and quantum communications [59,60].

The remainder of the paper is organized as follows. In Sec. II, we describe the theoretical model and the Hamiltonian of the ONF CQED system. In Sec. III, we describe the physical quantity of our interest, namely, the second-order intensity correlation function. Moreover, by means of both the master equation approach (Sec. III A) and the Schrödinger equation approach (Sec. III B), we yield insights into the numerical and analytical solutions of the second-order intensity correlation function, respectively. In Sec. IV, we demonstrate the experimental feasibility of our proposed scheme and the choice of typical ONF CQED system parameters. All parameters discussed here are readily achievable experimentally. In Sec. V, we investigate the relationship between the photon antibunching and the VIC and VIQB. Then, we compare the analytical solutions of the second-order intensity correlation function with the numerical solutions and find that they are in good agreement. Also, we analyze in detail the coherence statistics of photon antibunching by adjusting the typical system parameters. Finally, we summarize our results and yield our outlook in Sec. VI. In the Appendix, we present the Heisenberg-Langevin equation of motion governing the quantum beat dynamics for better readability.

II. PHYSICAL SYSTEM AND THEORETICAL FRAMEWORK

Figure 1 shows the schematic diagram for a coupled ONF CQED system that consists of a single three-level V-type atom inside a tapered ONF-based cavity. To be specific, the ONF cavity mode couples the $|2\rangle \leftrightarrow |0\rangle$ excited transition with frequency detuning $\Delta_c = \omega_{20} - \omega_c$ (ω_{20} is the excited resonance frequency of the $|2\rangle \leftrightarrow |0\rangle$ excited transition and ω_c is the resonance frequency of the ONF cavity mode). Again, the free-space control laser drives the $|1\rangle \leftrightarrow |0\rangle$ excited transition with Rabi frequency Ω in the vertical direction (axis x) and $\Delta = \omega_{10} - \omega$ is the control frequency detuning (ω_{10} is the excited resonance frequency of the $|1\rangle \leftrightarrow |0\rangle$ excited transition and ω is the central frequency of the control laser). The damping rate of atomic levels generated by the second-order coupling between $|i\rangle$ and $|j\rangle$ ($i, j = 1, 2$) is $\Gamma_{ij} = \vec{d}_{i0} \cdot \vec{d}_{j0} \omega_{i0}^3 / (3\pi \epsilon_0 \hbar c^3)$ [4], where the indices i, j refer to the atomic levels, \vec{d}_{i0} and ω_{i0} are the transition electric-dipole moment and the excited resonance frequency between $|i\rangle$ and $|0\rangle$ (the same is true for \vec{d}_{j0}), ϵ_0 is the permittivity of vacuum, \hbar is the reduced Planck constant, and c is the speed of light. Γ_{12} represents the cross-damping rate between the excited states $|1\rangle$ and $|2\rangle$, namely, the VIC as mentioned in Ref. [4], whereas Γ_{11} and Γ_{22} are the damping rates of the excited states $|1\rangle$ and $|2\rangle$ to the ground state $|0\rangle$, respectively. We can assume that all the transition dipole moments are parallel to each other and real, and obtain $\Gamma_{12} \simeq \sqrt{\Gamma_{11}\Gamma_{22}}$ like Refs. [4,61]. The ONF CQED system is coherently driven by an external laser field with the central frequency ω_p and the amplitude E_p through the damping rate κ_{e1} of the left-hand cavity mirror in the horizontal axial direction (axis z) and $\Delta_p = \omega_c - \omega_p$ is its frequency detuning from the resonance frequency ω_c of the cavity mode. In this circumstance, the light is coherently absorbed by the three-level atom (the small gold sphere) and reemitted into the cavity. Through the damping rate κ_{e2} of the right-hand cavity mirror, we can probe the statistical characteristics of the transmitted field by measuring the normalized second-order intensity correlation function $g^{(2)}(0)$.

Under the electric-dipole and rotating-wave approximations, the total Hamiltonian of the composite system which describes the atom-field coupling reads (assuming the Hamiltonian will be taken to have units of frequency here and hereafter)

$$\begin{aligned} \hat{H}_{\text{tot}} = & \omega_c \hat{a}^\dagger \hat{a} + \omega_{10} \hat{\sigma}_{11} + \omega_{20} \hat{\sigma}_{22} + g(\hat{a}^\dagger \hat{\sigma}_{02} + \hat{a} \hat{\sigma}_{02}^\dagger) \\ & + \Omega(e^{-i\omega t} \hat{\sigma}_{01}^\dagger + e^{i\omega t} \hat{\sigma}_{01}) + i(\eta e^{-i\omega_p t} \hat{a}^\dagger - \eta^* e^{i\omega_p t} \hat{a}), \end{aligned} \quad (1)$$

where \hat{a}^\dagger and \hat{a} are the creation and annihilation operators for photons inside the ONF cavity, obeying the bosonic commutation relations $[\hat{a}, \hat{a}^\dagger] = 1$, $[\hat{a}^\dagger, \hat{a}^\dagger] = 0$, and $[\hat{a}, \hat{a}] = 0$. $\hat{\sigma}_{lm} = |l\rangle\langle m|$ ($l, m = 0, 1, 2$) represents the raising ($l > m$), lowering ($l < m$), or population ($l = m$) operator for the atom. Notice that the relationship $\hat{\sigma}_{lm}^\dagger = |m\rangle\langle l| = \hat{\sigma}_{ml}$ holds. $g = d_{20} \sqrt{\omega_c / (2\hbar \epsilon_0 V)}$ is the cavity-atom coupling strength for the transition $|2\rangle \leftrightarrow |0\rangle$, where d_{20} is the electric-dipole moment of the corresponding transition $|2\rangle \leftrightarrow |0\rangle$ and V is the mode volume of the ONF cavity. $\Omega = d_{10} E / (2\hbar)$ is the Rabi frequency for the transition $|1\rangle \leftrightarrow |0\rangle$, where d_{10} is the

electric-dipole moment of the corresponding transition $|1\rangle \leftrightarrow |0\rangle$ and E is the field amplitude of the control laser. It should be pointed out that our definition of the control laser Rabi frequency Ω corresponds to half of the standard definition of Rabi frequency. Lastly, $\eta = \sqrt{\kappa_{e1}} E_p = \sqrt{P_p \kappa_{e1} / (\hbar \omega_p)}$ is the strength of the external driving laser to motivate the cavity mode \hat{a} , where P_p is the pump power of the external driving laser [62,63].

Several remarks are in order. First, it is pointed out that, for the first term of \hat{H}_{tot} [see Eq. (1)], the zero-point energy $\omega_c/2$ of the ONF cavity field is neglected. This is allowed because it only gives a relative shift and has no impact on the system dynamics. Second, for the second and third terms of \hat{H}_{tot} , the energy of the atomic ground state $|0\rangle$ is taken as the zero of energy for the sake of convenience. Third, the time dependencies of the fifth and sixth terms reflect that the energy of the system is not conserved. Such time dependencies are justified because the photons are exchanged with the external control and driving laser fields.

Below, for the purpose of eliminating the explicit temporal dependence in the total Hamiltonian \hat{H}_{tot} in Eq. (1) above, we perform a unitary transformation to a rotating coordinate frame described by the unitary operator $\hat{U}(t) = \exp(-i\hat{H}_0 t)$, where $\hat{H}_0 = \omega_p \hat{a}^\dagger \hat{a} + \omega \hat{\sigma}_{11} + \omega_p \hat{\sigma}_{22}$. Then, in terms of the formula $\hat{H}_{\text{rot}} = \hat{U}^\dagger(t) \hat{H}_{\text{tot}} \hat{U}(t) - i\hat{U}^\dagger(t) \partial \hat{U}(t) / \partial t$ [64], we can derive a time-independent effective Hamiltonian of the ONF CQED system after some algebra, with the form

$$\begin{aligned} \hat{H}_{\text{rot}} = & \Delta_p \hat{a}^\dagger \hat{a} + \Delta \hat{\sigma}_{11} + (\Delta_p + \Delta_c) \hat{\sigma}_{22} \\ & + g(\hat{a}^\dagger \hat{\sigma}_{02} + \hat{a} \hat{\sigma}_{02}^\dagger) + \Omega(\hat{\sigma}_{01}^\dagger + \hat{\sigma}_{01}) \\ & + i(\eta \hat{a}^\dagger - \eta^* \hat{a}), \end{aligned} \quad (2)$$

where the notation $\Delta_p = \omega_c - \omega_p$ is the detuning of the resonance frequency ω_c of the cavity mode from the driving laser frequency ω_p (named the driving detuning). $\Delta = \omega_{10} - \omega$ is the detuning of the excited resonance frequency ω_{10} from the control laser frequency ω (named the control detuning). $\Delta_c = \omega_{20} - \omega_c$ is the detuning of the excited resonance frequency ω_{20} from the resonance frequency ω_c of the cavity mode.

III. CALCULATIONS OF THE SECOND-ORDER INTENSITY CORRELATION FUNCTION

A. Numerical solutions via the full master equation approach

For the sake of treating the incoherent (dissipative) processes and describing the complete dynamics of the ONF CQED system with the joint atom-cavity density matrix operator $\hat{\rho}$, we can employ the Lindblad master equation in the Born-Markov approximation [4,64–67],

$$\begin{aligned} \frac{\partial \hat{\rho}}{\partial t} = & -i[\hat{H}_{\text{rot}}, \hat{\rho}] + \kappa \mathcal{D}(\hat{a}) \hat{\rho} + \Gamma_{11} \mathcal{D}(\hat{\sigma}_{01}) \hat{\rho} + \Gamma_{22} \mathcal{D}(\hat{\sigma}_{02}) \hat{\rho} \\ & + \Gamma_{12} (\hat{\sigma}_{01} \hat{\rho} \hat{\sigma}_{02}^\dagger - \hat{\sigma}_{02}^\dagger \hat{\sigma}_{01} \hat{\rho} / 2 - \hat{\rho} \hat{\sigma}_{02}^\dagger \hat{\sigma}_{01} / 2) \\ & + \Gamma_{12} (\hat{\sigma}_{02} \hat{\rho} \hat{\sigma}_{01}^\dagger - \hat{\sigma}_{01}^\dagger \hat{\sigma}_{02} \hat{\rho} / 2 - \hat{\rho} \hat{\sigma}_{01}^\dagger \hat{\sigma}_{02} / 2), \end{aligned} \quad (3)$$

with \hat{H}_{rot} being the effective Hamiltonian directly yielded by Eq. (2) and the brackets $[\cdot, \cdot]$ denoting the commutator. $\mathcal{D}(\hat{O}) \hat{\rho} = \hat{O} \hat{\rho} \hat{O}^\dagger - \hat{O}^\dagger \hat{O} \hat{\rho} / 2 - \hat{\rho} \hat{O}^\dagger \hat{O} / 2$ is a standard Lindblad operator form for the collapse operator \hat{O} , accounting

for the dissipation to the environment. Here, κ is the total damping rate of the cavity (i.e., $\kappa = \kappa_{e1} + \kappa_{e2} + \kappa_i$). Γ_{11} and Γ_{22} are the damping rates of the excited states $|1\rangle$ and $|2\rangle$ to the ground state $|0\rangle$, respectively. Γ_{12} represents the VIC. The first term on the right-hand side of Eq. (3) denotes the coherent evolution of the whole system. The second term represents the coupling of the cavity mode with the environment with the damping rate κ . The third term shows the dissipation of the excited state $|1\rangle$ into the environment with the damping rate Γ_{11} . The fourth term describes the dissipation of the excited state $|2\rangle$ into the environment with the damping rate Γ_{22} . Finally, the last two terms illustrate the dissipative coupling between the excited states $|1\rangle$ and $|2\rangle$ into the environment with the VIC (i.e., Γ_{12}) [4].

By applying the standard input-output formalism [68,69], we can define the operator \hat{S}_{out} describing the transmitted field through the right-hand cavity mirror and arrive at the continuity relation $\dot{\hat{S}}_{\text{out}} = \sqrt{\kappa_{e2}}\hat{a}$, with κ_{e2} being the damping rate of the right-hand cavity mirror. For a rotating-frame time-independent Hamiltonian \hat{H}_{rot} [see Eq. (2)], the dynamics of the system evolves into a steady state as $t \rightarrow \infty$ corresponding to $\partial\hat{\rho}/\partial t = 0$. In this case, the statistical properties of the transmitted field can be characterized by the normalized delayed second-order intensity correlation function [70], which is defined by

$$g^{(2)}(\tau) = \frac{\langle \hat{S}_{\text{out}}^\dagger(t)\hat{S}_{\text{out}}^\dagger(t+\tau)\hat{S}_{\text{out}}(t+\tau)\hat{S}_{\text{out}}(t) \rangle}{\langle \hat{S}_{\text{out}}^\dagger(t)\hat{S}_{\text{out}}(t) \rangle^2} = \frac{\langle \hat{a}^\dagger(t)\hat{a}^\dagger(t+\tau)\hat{a}(t+\tau)\hat{a}(t) \rangle}{\langle \hat{a}^\dagger(t)\hat{a}(t) \rangle^2}, \quad (4)$$

where $\langle \cdot \rangle$ represents the expectation value of the operator and τ is the delay time between different detectors. Here, the normalized equal-time (or zero-time-delay $\tau = 0$) second-order intensity correlation function can be expressed as [70]

$$g^{(2)}(0) = \frac{\langle \hat{a}^\dagger \hat{a}^\dagger \hat{a} \hat{a} \rangle}{\langle \hat{a}^\dagger \hat{a} \rangle^2} = \frac{\text{Tr}(\hat{\rho}_{ss} \hat{a}^\dagger \hat{a}^\dagger \hat{a} \hat{a})}{[\text{Tr}(\hat{\rho}_{ss} \hat{a}^\dagger \hat{a})]^2}, \quad (5)$$

where Tr means the trace and $\hat{\rho}_{ss}$ is the steady-state solution of the density matrix $\hat{\rho}$ for the coupled ONF CQED system by numerically solving the Lindblad master equation (3) under $\partial\hat{\rho}_{ss}/\partial t = 0$, with the constraint $\text{Tr}(\hat{\rho}_{ss}) = 1$.

The signature of the photon antibunching and bunching can be distinguished by measuring the second-order intensity correlation function from the output of the optical cavity [70,71]. The photon antibunching effect with $g^{(2)}(0) < 1$ [or $g^{(2)}(\tau) > g^{(2)}(0)$] indicates that the transmitted light is sub-Poissonian and antibunched. The limit $g^{(2)}(0) \rightarrow 0$ means a complete photon blockade phenomenon [72]. The smallness of $g^{(2)}(0)$ is considered as the quality of photon antibunching, which is also directly related to the single-photon purity P by the relation $P = 1 - g^{(2)}(0)$ [73,74]. According to the second-order intensity correlation function, we can judge whether photon antibunching happens or not. In contrast, if $g^{(2)}(0) > 1$ [or $g^{(2)}(\tau) < g^{(2)}(0)$], the transmitted light shows super-Poissonian and bunched corresponding to the photon bunching effect. In particular, the value of $g^{(2)}(0) = 1$ corresponds to Poissonian photon statistics, which is a quasicalssical effect.

Here, the normalized second-order intensity correlation function $g^{(2)}(0)$ can be calculated by numerically solving the master equation (3) within a truncated Fock space. To do so, we consider a Hilbert space expanded by the three electronic states of the atom and the Fock states of the ONF cavity. Notice that the dynamics of the considered ONF CQED system evolves towards a steady state $\hat{\rho}_{ss}$ after long enough time, where the condition $\partial\hat{\rho}_{ss}/\partial t = 0$ holds. In the numerical simulations, we can truncate the Hilbert space at photon numbers as low as 10 for the ONF cavity mode [72], which is sufficient to guarantee the convergence of the simulations. Again, the convergence of our numerical simulations can be checked by varying the cutoff number of the ONF cavity photons [75]. The cutoff number of photons as low as 10 for the ONF cavity mode corresponds to a total Hilbert space of 30 for the ONF CQED system and hence such a master equation for the steady-state density matrix [i.e., Eq. (3)] equivalent to a linear system of 900 equations [76]. Hence the dynamic characteristics of the ONF CQED system are obtained by the numerical diagonalization. The details of the numerical results will be discussed in Sec. V below.

Before continuing, it should be pointed out that seeking the analytical solutions of the normalized second-order intensity correlation function can help us to better explore the photon antibunching effect in the ONF CQED system and to gain further insight into the physics at play. To this end, we will first discuss how to analytically calculate the second-order intensity correlation function $g^{(2)}(0)$ in the next section (Sec. III B).

B. Analytical solutions via the Schrödinger equation approach

In what follows, for the purpose of better exploring the photon antibunching effect in the ONF CQED system, in this section, we present approximate analytical expressions for the second-order intensity correlation function $g^{(2)}(0)$ of the transmitted field. Under the scenario of weak driving ($\eta \ll g, \kappa$), the population of the high-photon excitation states is so low that the total excitation number of the atom-cavity system can be assumed to not exceed two, like in Refs. [43,77]. In this circumstance, the wave function of the atom-cavity system can be reasonably approximated in the two-excitation manifold with the ansatz [43,78]

$$|\Psi(t)\rangle \simeq C_{00}|0_s, 0\rangle + C_{01}|0_s, 1\rangle + C_{02}|0_s, 2\rangle + C_{10}|1_s, 0\rangle + C_{11}|1_s, 1\rangle + C_{20}|2_s, 0\rangle + C_{21}|2_s, 1\rangle, \quad (6)$$

where $|m, n\rangle = |m\rangle \otimes |n\rangle$ denotes a tensor product of the atomic state $|m\rangle$ ($m = 0, 1, 2$; the subscript “s” of $|m\rangle$ is only for better visualization) in the three-level V-type atom and the photonic Fock state with $n = 0, 1, 2$ photons in the ONF cavity mode. The coefficient C_{mn} stands for the probability amplitude of the corresponding state $|m, n\rangle$, for which the corresponding probability is given by $|C_{mn}|^2$. In the limit of weak driving, we have the relationship $C_{00} \gg \{C_{01}, C_{10}, C_{20}\} \gg \{C_{02}, C_{11}, C_{21}\}$.

Again, under the weak-driving limit, the atom-cavity system remains predominantly in the ground state. As a result, the contributions of the $2\hat{a}\hat{\rho}\hat{a}^\dagger$ and $2\delta_{lm}\hat{\rho}\delta_{lm}^\dagger$ ($l, m = 0, 1, 2$) terms appearing in the Lindblad master equation can be safely ignored [79,80]. This just is equivalent to obtaining the

effective non-Hermitian Hamiltonian

$$\begin{aligned} \hat{H}_{\text{eff}} = & (\Delta_p - i\kappa/2)\hat{a}^\dagger\hat{a} + (\Delta - i\Gamma_{11}/2)\hat{\sigma}_{11} \\ & + (\Delta_p + \Delta_c - i\Gamma_{22}/2)\hat{\sigma}_{22} - i\Gamma_{12}(\hat{\sigma}_{12} + \hat{\sigma}_{21})/2 \\ & + g(\hat{a}^\dagger\hat{\sigma}_{02} + \hat{a}\hat{\sigma}_{02}^\dagger) + \Omega(\hat{\sigma}_{01}^\dagger + \hat{\sigma}_{01}) + i(\eta\hat{a}^\dagger - \eta^*\hat{a}), \end{aligned} \quad (7)$$

where, for the fourth term (i.e., the VIC between both radiative channels), we can find that its coupling strength is imaginary which is a characteristic of dissipative coupling. Physically, the imaginary parts of the second and third terms indicate that the coupling of the two quantum transition pathways with a common reservoir results in the dampings Γ_{11} and Γ_{22} , respectively. The relation $\Gamma_{12} \simeq \sqrt{\Gamma_{11}\Gamma_{22}}$ indicates that the coupling with the common reservoir induces a dissipative coupling between these two radiative channels [4].

Based on the time-dependent Schrödinger equation $i\partial|\Psi\rangle/\partial t = \hat{H}_{\text{eff}}|\Psi\rangle$, the dynamics of the above probability amplitude coefficients C_{mn} can be described by a set of coupled equations as follows (overdots indicate time derivatives):

$$i\dot{C}_{00} = \Omega C_{10} - i\eta^* C_{01}, \quad (8)$$

$$\begin{aligned} i\dot{C}_{01} = & (\Delta_p - i\kappa/2)C_{01} + gC_{20} + \Omega C_{11} + i\eta C_{00} \\ & - i\sqrt{2}\eta^* C_{02}, \end{aligned} \quad (9)$$

$$i\dot{C}_{02} = 2(\Delta_p - i\kappa/2)C_{02} + \sqrt{2}gC_{21} + i\sqrt{2}\eta C_{01}, \quad (10)$$

$$i\dot{C}_{10} = (\Delta - i\Gamma_{11}/2)C_{10} - i\Gamma_{12}C_{20}/2 + \Omega C_{00} - i\eta^* C_{11}, \quad (11)$$

$$\begin{aligned} i\dot{C}_{11} = & (\Delta_p + \Delta - i\kappa/2 - i\Gamma_{11}/2)C_{11} - i\Gamma_{12}C_{21}/2 \\ & + \Omega C_{01} + i\eta C_{10}, \end{aligned} \quad (12)$$

$$\begin{aligned} i\dot{C}_{20} = & (\Delta_p + \Delta_c - i\Gamma_{22}/2)C_{20} - i\Gamma_{12}C_{10}/2 + gC_{01} \\ & - i\eta^* C_{21}, \end{aligned} \quad (13)$$

$$\begin{aligned} i\dot{C}_{21} = & (2\Delta_p + \Delta_c - i\kappa/2 - i\Gamma_{22}/2)C_{21} - i\Gamma_{12}C_{11}/2 \\ & + \sqrt{2}gC_{02} + i\eta C_{20}. \end{aligned} \quad (14)$$

In the steady-state case by setting the left-hand sides of Eqs. (8)–(14) to zero (i.e., $\dot{C}_{mn} = 0$), the following set of coupled linear equations for the probability ampli-

tude coefficients C_{mn} can be obtained thereby, with the forms

$$0 = \Omega C_{10} - i\eta^* C_{01}, \quad (15)$$

$$0 = (\Delta_p - i\kappa/2)C_{01} + gC_{20} + \Omega C_{11} + i\eta C_{00} - i\sqrt{2}\eta^* C_{02}, \quad (16)$$

$$0 = 2(\Delta_p - i\kappa/2)C_{02} + \sqrt{2}gC_{21} + i\sqrt{2}\eta C_{01}, \quad (17)$$

$$0 = (\Delta - i\Gamma_{11}/2)C_{10} - i\Gamma_{12}C_{20}/2 + \Omega C_{00} - i\eta^* C_{11}, \quad (18)$$

$$\begin{aligned} 0 = & (\Delta_p + \Delta - i\kappa/2 - i\Gamma_{11}/2)C_{11} - i\Gamma_{12}C_{21}/2 \\ & + \Omega C_{01} + i\eta C_{10}, \end{aligned} \quad (19)$$

$$0 = (\Delta_p + \Delta_c - i\Gamma_{22}/2)C_{20} - i\Gamma_{12}C_{10}/2 + gC_{01} - i\eta^* C_{21}, \quad (20)$$

$$\begin{aligned} 0 = & (2\Delta_p + \Delta_c - i\kappa/2 - i\Gamma_{22}/2)C_{21} - i\Gamma_{12}C_{11}/2 \\ & + \sqrt{2}gC_{02} + i\eta C_{20}. \end{aligned} \quad (21)$$

Owing to the weak-cavity-driving limit, the probability of finding two photons in the ONF cavity is very small, such that they can be safely ignored relative to the probability of finding one (i.e., $C_{00} \gg \{C_{01}, C_{10}, C_{20}\} \gg \{C_{02}, C_{11}, C_{21}\}$). Additionally, it is reasonable to assume that the vacuum state is approximately occupied with probability 1 as in Ref. [81]. That is to say, we can assume $C_{00} \sim 1$, $\eta C_{02} \sim 0$, $\eta C_{11} \sim 0$, and $\eta C_{21} \sim 0$ like in Ref. [82]. Based on the above reasonable assumptions, by recurrently solving Eqs. (15)–(21), we can obtain the concrete expressions for the probability amplitude coefficients C_{mn} . Then the normalized equal-time second-order intensity correlation function based on these coefficients C_{mn} can be approximated by

$$g^{(2)}(0) = \frac{\langle \Psi | \hat{a}^\dagger \hat{a}^\dagger \hat{a} \hat{a} | \Psi \rangle_{ss}}{\langle \Psi | \hat{a}^\dagger \hat{a} | \Psi \rangle_{ss}^2} \simeq \frac{2|C_{02}|^2}{|C_{01}|^4}, \quad (22)$$

where the subscript “ss” denotes the expectation values taken with respect to the steady-state solution, and accordingly $|\Psi\rangle$ is the steady-state wave function of the ONF CQED system. In general, the analytical expressions of C_{mn} are complex. For the sake of simplicity, we introduce three effective detunings, defined as $\Delta'_p = \Delta_p - i\kappa/2$, $\Delta' = \Delta - i\Gamma_{11}/2$, and $\Delta'_c = \Delta_p + \Delta_c - i\Gamma_{22}/2$, which take into account the presence of damping rates in the system. Furthermore, for simplicity of calculation, only C_{01} and C_{02} are given as below:

$$C_{01} = \frac{i(-16\eta\Delta'_c X_{01} + 8g\eta Y_{01}\Gamma_{12} + 4\eta Z_{01}\Gamma_{12}^2 + 2g\Omega\Delta'_p\Gamma_{12}^3 - \eta\Delta'_p\Gamma_{12}^4)}{16\Delta'A + 8g\eta\Omega B\Gamma_{12} + 4C\Gamma_{12}^2 - 2g\eta\Omega\Gamma_{12}^3 + \Delta_p'^2\Gamma_{12}^4}, \quad (23)$$

$$C_{02} = \frac{-16\eta^2 X_{02} - 8g\eta\Omega Y_{02}\Gamma_{12} + 4Z_{02}\Gamma_{12}^2 + 4g\eta\Omega\Gamma_{12}^3 - \eta^2\Gamma_{12}^4}{\sqrt{2}(16\Delta'A + 8g\eta\Omega B\Gamma_{12} + 4C\Gamma_{12}^2 - 2g\eta\Omega\Gamma_{12}^3 + \Delta_p'^2\Gamma_{12}^4)}, \quad (24)$$

where

$$\begin{aligned}
 A &= [g^2 - \Delta'_p(\Delta'_p + \Delta'_c)][\Omega^2 \Delta'_c + (\Delta'_p + \Delta') (g^2 - \Delta'_p \Delta'_c)], \\
 B &= g^2 - (\Delta'_p + \Delta')(\Delta'_p + \Delta'_c), \\
 C &= \Delta'_p \Delta' (-2g^2 + 2\Delta'_p \Delta'_c + \Delta'_p{}^2) - (\Omega - \Delta'_p)(\Omega + \Delta'_p)[-g^2 + \Delta'_p(\Delta'_p + \Delta'_c)], \\
 X_{01} &= [\Omega^2 + \Delta'(\Delta'_p + \Delta')][-g^2 + \Delta'_p(\Delta'_p + \Delta'_c)], \\
 Y_{01} &= (\Delta'_p + \Delta')[-g^2 + \Delta'_p(\Delta'_p + \Delta'_c)], \\
 Z_{01} &= \Delta'_p[g^2 + \Omega^2 - \Delta'_p(\Delta'_p + \Delta'_c)] + \Delta'[g^2 - \Delta'_p(\Delta'_p + 2\Delta'_c)], \\
 X_{02} &= [\Omega^2 + \Delta'(\Delta'_p + \Delta')][g^2 + \Delta'_c(\Delta'_p + \Delta'_c)], \\
 Y_{02} &= g^2 + \Omega^2 - 2(\Delta'_p + \Delta')(\Delta'_p + \Delta'_c), \\
 Z_{02} &= \eta^2 \Omega^2 + g^2(\eta - \Omega)(\eta + \Omega) - \eta^2[\Delta'_p(\Delta'_p + \Delta'_c) + \Delta'(\Delta'_p + 2\Delta'_c)].
 \end{aligned} \tag{25}$$

According to Eqs. (22)–(25), the detailed analytical expression of the second-order intensity correlation function $g^{(2)}(0)$ can be obtained. However, the analytical expression of the second-order intensity correlation function $g^{(2)}(0)$ is too cumbersome to offer clear physical insight (not presented here). Yet, it is not difficult to find that the statistical property of photons is closely related to the VIC [i.e., Γ_{12} ; cf. Eqs. (23) and (24)]. Again, based on Eqs. (8)–(14), we present the schematic diagram of the energy level showing the zero-, one-, and two-photon states and the transition pathways of the coupled ONF CQED system, as shown in Fig. 2. It is worth emphasizing from Fig. 2 that, thanks to the introduction of the VIC, quantum interference can occur between different two-photon excitation pathways, as marked by the red double arrows of Fig. 2.

IV. EXPERIMENTAL FEASIBILITY AND TYPICAL PARAMETERS FOR THE MODEL

Before proceeding, we briefly address the experimental feasibility of our scheme. In accordance with the experimental report in Ref. [4], we can employ a single ^{85}Rb atom (nuclear spin $I = 5/2$, D_2 line, and wavelength 780 nm) on the $5^2S_{1/2} \rightarrow 5^2P_{3/2}$ transition as a possible candidate [83] for the ONF CQED system. The designated three-level V -type atomic states can be chosen as follows: The ground state $|0\rangle = |5^2S_{1/2}, F = 3\rangle$, and the two excited states $|1\rangle = |5^2P_{3/2}, F = 4\rangle$ and $|2\rangle = |5^2P_{3/2}, F = 3\rangle$ (see Fig. 1), where F is the total angular momentum quantum number and marks the hyperfine state. The damping rates of the excited states $|1\rangle$ and $|2\rangle$ to the ground state $|0\rangle$ are $\Gamma_{11} = 2\pi \times 6.1$ MHz and $\Gamma_{22} = 5/9 \times 2\pi \times 6.1$ MHz, respectively. The branching ratio for a decay from $|2\rangle$ to $|0\rangle$ is $5/9$ [4,83,84]. The cross-damping rate between the excited states $|1\rangle$ and $|2\rangle$ is $\Gamma_{12} \simeq \sqrt{\Gamma_{11}\Gamma_{22}} = \sqrt{5/9} \times 2\pi \times 6.1$ MHz (assuming that all the transition dipole moments are parallel to each other and real) [4]. In recent years, VIC has been investigated theoretically in several single-atom systems, such as V -type systems [85,86], Λ -type systems [87], and ladder-type systems [88], and has been demonstrated experimentally in atomic ensembles [4,25,89,90] where the single-atom approximation

has been adopted in the theoretical model of fitting. In the multiatom systems, the interference effect arising from the VIC between the two closely spaced excited levels has been well demonstrated experimentally [89]. It is reasonable to anticipate that the experimental demonstration of VIC in the

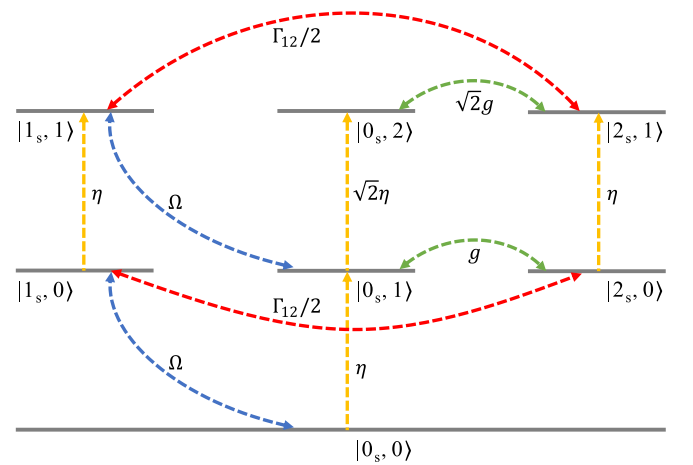


FIG. 2. Schematic diagram of the energy levels showing the zero-, one-, and two-photon states (horizontal gray lines without arrows) and the transition pathways (color lines with arrows) of the coupled ONF CQED system. States are marked as $|m, n\rangle$, where the first number $m = 0, 1, 2$ corresponds to the state of the three-level atom and the second number represents the photonic Fock state for the cavity mode with the photon number $n = 0, 1, 2$. The yellow double arrows mean the different energy-level transitions caused by the coupling of the external driving laser with the strength η . The green double arrows represent the different energy-level transitions resulting from the cavity-atom coupling g . The blue double arrows denote the different energy-level transitions as a result of the Rabi frequency Ω . The red double arrows indicate the different energy-level transitions induced by the VIC (i.e., Γ_{12}). When the different energy-level transitions induced by the VIC (the red double arrows) exist, the VIQB can occur. The emergence of the VIQB demonstrates the existence of quantum interference in the ONF CQED system, which can enable unconventional photon antibunching based on the destructive quantum interference between the different transition pathways.

single-atom systems may further reveal the interaction between the two closely spaced excited levels, which may have potential applications in quantum optics.

A tapered ONF-based cavity provides a unique fiber-in-line platform for the ONF CQED system [56]. The tapered ONF can be fabricated by adiabatically tapering commercial single-mode optical fiber using a heat-and-pull technique [55]. The ONF-based cavity can be formed by laser-writing two fiber Bragg gratings (FBGs) into the ONF using a focused ion beam milling technique [91,92], termed the FBG nanofiber cavity, or by introducing two photonic crystal (PC) defect structures into the ONF using a femtosecond laser ablation technique [93,94], termed the PC nanofiber cavity. The FBG-PC nanofiber cavity by combining the above two approaches has also been reported in Ref. [56]. On the other hand, a single atom trapped in the vicinity of the ONF can be achieved with several techniques [54,56,95–99].

For our proposed ONF CQED system consisting of a single ^{85}Rb atom confined in a tapered ONF-based cavity, the resonance frequency ω_c of the cavity mode can be modulated to be near resonance with the transition frequency ω_{20} of the excited transition $|2\rangle \leftrightarrow |0\rangle$, that is, $\omega_c = \omega_{20} = 2\pi c/\lambda$ (c is the speed of light and λ is 780 nm). The ONF-based cavity field is a guided field with a small effective cross-section area. As a result, even when the finesse of the ONF-based cavity is moderate and the length of the ONF-based cavity is long, the interplay between the guided field and the atom can still be substantial [54,100]. The motivation behind the use of a nanofiber cavity is to controllably generate the guided-mode photon antibunching, which can be easily transmitted over a long distance for quantum communication purposes. For example, the cavity with the linewidth (the total damping rate of the ONF cavity mode) is $\kappa = 2\pi \times 6.4$ MHz (the damping rates of the left- and right-hand cavity mirrors $\kappa_{e1} = \kappa_{e2} = 2\pi \times 1.6$ MHz, and the inner damping rate $\kappa_i = 2\pi \times 3.2$ MHz), the length is $L = 33$ cm [54], and the finesse (roughly the number of intracavity photon round trips during the cavity decay time) is $F = \pi c/(\kappa L) = 71$. The cavity-atom coupling strength g for the excited transition $|2\rangle \leftrightarrow |0\rangle$ selected in this paper can be implemented in the experiment [54]. Specifically, the typical cavity-atom coupling strength $g = 2\pi \times (1.3, 1.9, 2.9, 4.3, 7.8)$ MHz is within a reasonable range of experimental parameters [54,100–102]. To sum up, all parameters discussed here for the implementation of our scheme are accessible experimentally.

V. RESULTS AND DISCUSSIONS ABOUT CORRELATION $g^{(2)}(0)$

First of all, we focus on the relationship between the photon antibunching and the quantum beat dynamics. We plot the normalized equal-time second-order intensity correlation function $g^{(2)}(0)$ as a function of the driving detuning $\Delta_p/2\pi$ in Figs. 3(a)–3(d) and the atomic population $\sigma_{22} = \langle \hat{\sigma}_{22} \rangle$ (i.e., the expectation value of the population operator $\hat{\sigma}_{22}$) as a function of time t in Figs. 3(e)–3(h), corresponding to the four different cases of $g/2\pi = 1.3$ MHz [see Figs. 3(a) and 3(e)], $g/2\pi = 2.9$ MHz [see Figs. 3(b) and 3(f)], $g/2\pi = 4.3$ MHz [see Figs. 3(c) and 3(g)], and $g/2\pi = 7.8$ MHz [see Figs. 3(d) and 3(h)]. The derivation of the atomic population

σ_{22} is detailed in the Appendix. The red dotted lines correspond to $g^{(2)}(0)$ and σ_{22} with VIC and the blue solid lines correspond to $g^{(2)}(0)$ and σ_{22} without VIC, respectively. In Figs. 3(e)–3(h), the left red vertical axis and the right blue vertical axis correspond to the red dotted lines and the blue solid lines, respectively. In order to more explicitly illustrate the relationship between the oscillation frequency and the cavity-atom coupling strength $g/2\pi$ in the VIQB [see the red dotted lines in the insets of Figs. 3(e)–3(h)], we can utilize the time difference Δt_n ($n = 1, 2, 3, 4$) between the first (orange dash-dotted vertical lines) and second (green dotted vertical lines) oscillation minimum of σ_{22} to provide a more intuitive view in the respective zoom-in regions. According to the four different cases of $g/2\pi = 1.3$ MHz [$\Delta t_1 = 1.30\mu\text{s}$; see Fig. 3(e)], $g/2\pi = 2.9$ MHz [$\Delta t_1 = 1.27\mu\text{s}$; see Fig. 3(f)], $g/2\pi = 4.3$ MHz [$\Delta t_1 = 1.12\mu\text{s}$; see Fig. 3(g)], and $g/2\pi = 7.8$ MHz [$\Delta t_1 = 0.86\mu\text{s}$; see Fig. 3(h)], it can be observed that the time difference between the first and second oscillation minimum of σ_{22} decreases as the cavity-atom coupling strength $g/2\pi$ gradually increases. It can be clearly seen from Figs. 3(a)–3(h) that the emergence of the VIQB [see the red dotted lines in Figs. 3(e)–3(h)] corresponds to the occurrence of the strong photon antibunching in a broad parameter region of the driving detuning [see the red dotted lines in Figs. 3(a)–3(d)]. On the contrary, when the VIQB disappears [see the blue solid lines in Figs. 3(e)–3(h)], the antibunching effect also vanishes [see the blue solid lines in Figs. 3(a)–3(d)] in the ONF CQED system. When the different energy-level transitions induced by the VIC (see the red double arrows in Fig. 2) exist, the VIQB can occur. The emergence of the VIQB demonstrates the existence of quantum interference in the ONF CQED system, which can realize unconventional photon antibunching based on the destructive quantum interference between the different transition pathways. That is to say, the VIQB can enable strong photon antibunching, which is useful for building a tunable single-photon source and enabling potential applications in quantum information processing and quantum communications.

When the VIQB exists (red dotted lines), in the weak-coupling regime [i.e., $g < (\kappa, \Gamma_1)$, where $\Gamma_1 = \Gamma_{11} + \Gamma_{12}$] [103], a strong antibunching can be observed on the center at $\Delta_p/2\pi = 0$ MHz for $g/2\pi = 1.3$ MHz [see Fig. 3(a)], where the value of $g^{(2)}(0)$ arrives at $g^{(2)}(0) \simeq 0.021$. The strong antibunching [$g^{(2)}(0) \simeq 0.021$] corresponds to a single-photon purity $P = 1 - g^{(2)}(0) = 0.979$ in the ONF CQED system [73,74]. Similarly, the strong antibunching [$g^{(2)}(0) \simeq 0.025$] can be observed on both sides around $\Delta_p/2\pi \simeq \pm 8.9$ MHz for $g/2\pi = 2.9$ MHz [see Fig. 3(b)] and the strong antibunching [$g^{(2)}(0) \simeq 0.013$] can be observed on both sides around $\Delta_p/2\pi \simeq \pm 11.6$ MHz for $g/2\pi = 4.3$ MHz [see Fig. 3(c)]. With increasing the cavity-atom coupling strength $g/2\pi$, entering into the strong-coupling regime (i.e., $g > \kappa$), the strong photon antibunching [$g^{(2)}(0) \simeq 0.003$] can also be observed on both sides around $\Delta_p/2\pi \simeq \pm 16$ MHz for $g/2\pi = 7.8$ MHz [see Fig. 3(d)]. Conversely, in the absence of the VIQB (blue solid lines), there is no antibunching effect [e.g., at $\Delta_p/2\pi = 0$ MHz in Fig. 3(c), $g^{(2)}(0) \simeq 5.3$ corresponds to the photon bunching].

Physically, the occurrence of the strong antibunching effect is due to the fact that the introduction of VIC adds a

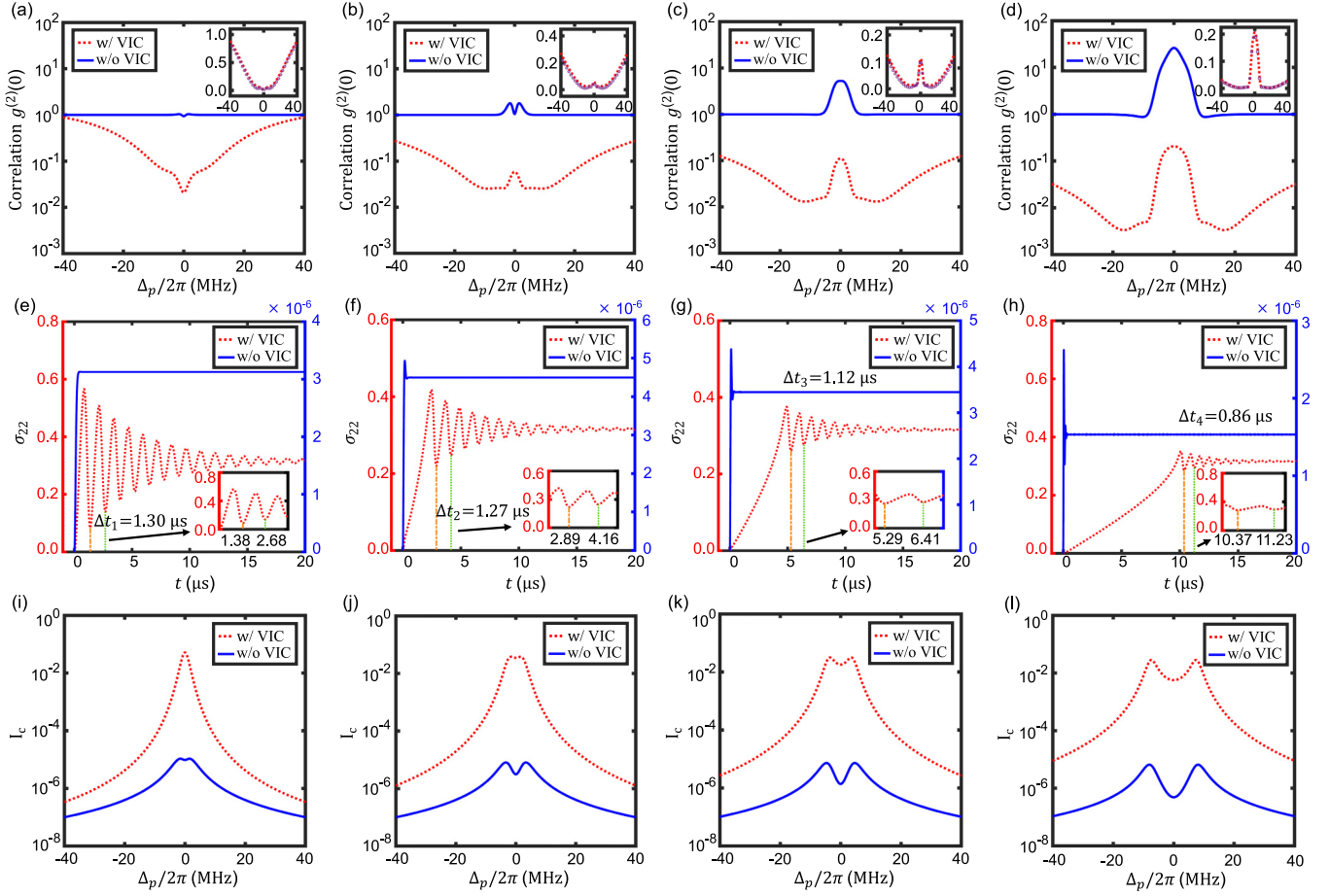


FIG. 3. [(a)–(d)] The normalized equal-time second-order intensity correlation function $g^{(2)}(0)$ as a function of the driving detuning $\Delta_p/2\pi$ with the VIC ($\Gamma_{12} = \sqrt{5/9} \times 2\pi \times 6.1$ MHz; red dotted lines) and without the VIC ($\Gamma_{12} = 0$; blue solid lines), corresponding to the four different cases (a) $g/2\pi = 1.3$ MHz, (b) $g/2\pi = 2.9$ MHz, (c) $g/2\pi = 4.3$ MHz, and (d) $g/2\pi = 7.8$ MHz. In the case with VIC, the comparisons between the numerical results [red dotted lines, calculated numerically by the quantum master equation (3)] and the analytical results [purple circles, calculated analytically by the closed-form expressions (22)–(25)] are shown in the insets, where the insets use the normal vertical axis to better display the fitting results. [(e)–(h)] The atomic population σ_{22} as a function of time t corresponding to (a)–(d), respectively. In (e)–(h), the left red vertical axis and the right blue vertical axis show the atomic population σ_{22} with VIC (red dotted lines) and without VIC (the blue solid lines) in the ONF CQED system, respectively. The orange dash-dotted vertical lines and the green dotted vertical lines show the time t corresponding to the first and second oscillation minimum of σ_{22} with VIC, respectively. Δt_n ($n = 1, 2, 3, 4$) represents the time difference between the first and second oscillation minimum of σ_{22} with VIC. The enlarged views of the first and second oscillation minimum of σ_{22} with VIC are shown in the insets, where the time abscissa axis in the insets only shows the time t corresponding to the first and second oscillation minimum for clarity and simplicity. [(i)–(l)] The intensity I_c of the ONF-based cavity emission light as a function of the driving detuning $\Delta_p/2\pi$ with VIC (red dotted lines) and without VIC (blue solid lines) corresponding to (a)–(d), respectively. The system parameters for all panels are chosen as $\kappa/2\pi = 6.4$ MHz, $\Gamma_{11}/2\pi = 6.1$ MHz, $\Gamma_{22}/2\pi = 5/9 \times 6.1$ MHz, $\Omega/2\pi = 0.65$ MHz, $\eta/2\pi = 0.01$ MHz, $\Delta/2\pi = 0$ MHz, and $\Delta_c/2\pi = 0$ MHz, typically from a recent experiment [4].

few additional transition pathways to the ONF CQED system and leads to the destructive quantum interference between different transition pathways for two-photon excitation. As displayed in Fig. 2, quantum interference can occur between the two different two-photon excitation pathways. More specifically, pathway (i) involves direct input of two photons into the cavity mode via the external driving, which we refer to as the direct pathway, i.e., $|0_s, 0\rangle \xrightarrow{\eta} |0_s, 1\rangle \xrightarrow{\sqrt{2}\eta} |0_s, 2\rangle$; and pathway (ii) is the indirect pathway facilitated by the control field and the VIC, i.e., $|0_s, 0\rangle \xrightarrow{\Omega} |1_s, 0\rangle \xrightarrow{\eta} |1_s, 1\rangle \xrightarrow{\Gamma_{12}/2} |2_s, 1\rangle \xrightarrow{\sqrt{2}g} |0_s, 2\rangle$. In order to illustrate the influence of the

introduction of VIC (i.e., Γ_{12}) on the indirect pathway (i.e., $|1_s, 1\rangle \xrightarrow{\Gamma_{12}/2} |2_s, 1\rangle$), through numerical calculations, we can obtain the probabilities $|C_{11}|^2$ and $|C_{21}|^2$ corresponding to the states $|1_s, 1\rangle$ and $|2_s, 1\rangle$, respectively. For example, when $g/2\pi = 2.9$ MHz and $\Delta_p/2\pi = 0$ MHz [see Fig. 3(b)], in the absence of VIC, the probabilities are $|C_{11}|^2 = 2.2 \times 10^{-7}$ and $|C_{21}|^2 = 1.7 \times 10^{-11}$, indicating that the probability of the state $|2_s, 1\rangle$ is four orders of magnitude smaller than that of the state $|1_s, 1\rangle$. However, in the presence of the VIC, the probabilities are $|C_{11}|^2 = 4.1 \times 10^{-4}$ and $|C_{21}|^2 = 3.8 \times 10^{-5}$, where the probability of the state $|2_s, 1\rangle$ is only one order of magnitude smaller than that of the state $|1_s, 1\rangle$. The

discrepancy in the reductions between the probabilities $|C_{11}|^2$ and $|C_{21}|^2$ from four orders of magnitude (without VIC) to one order of magnitude (with VIC) verifies the role of VIC in bridging the photon transfer from state $|1_s, 1\rangle$ to state $|2_s, 1\rangle$ (i.e., $|1_s, 1\rangle \xrightarrow{\Gamma_{12}/2} |2_s, 1\rangle$; see the red double arrows in Fig. 2). The important influence of VIC on the photon transfer from state $|1_s, 1\rangle$ to state $|2_s, 1\rangle$ can also be seen from the process of calculating the probability amplitude C_{21} [see Eq. (14)] [82]. By introducing VIC, the photon transfer from state $|1_s, 1\rangle$ to state $|2_s, 1\rangle$ (i.e., $|1_s, 1\rangle \xrightarrow{\Gamma_{12}/2} |2_s, 1\rangle$) can be constructed, which has potential significance in energy transfer studies [104–106]. As foreseen, the pathway $|1_s, 1\rangle \xrightarrow{\Gamma_{12}/2} |2_s, 1\rangle$ can also be bridged by a coherent microwave or radio frequency (RF) field. The difference in both approaches is that the VIC is incoherent (dissipative) while the microwave- or RF-based coupling is coherent. Unlike the previous works [42,43] on cavity-coupling cavity-induced quantum interference, the photons from both pathways (i) and (ii) cannot occupy the two-photon state $|0_s, 2\rangle$ due to the interference of these two excitation pathways. In other words, the destructive quantum interference between different transition pathways can reduce the probability in the two-photon excited state. As a consequence, the strong antibunching effect induced by the quantum interference can be realized. It is worth stressing that the above results can be based on the weak-coupling regime of CQED [see Figs. 3(a)–3(c)], highlighting the crucial role of VIC in the pathway interference.

In addition, the comparisons between the numerical and analytical results for the normalized equal-time second-order intensity correlation function $g^{(2)}(0)$ with VIC are revealed in the insets of Figs. 3(a)–3(d). The red dotted lines and the purple circles correspond to the numerical simulation results given by the master equation (3) and the analytical results given by the closed-form expressions (22)–(25) based on the Schrödinger equation in the steady state, respectively. The insets show that the numerical simulation results for $g^{(2)}(0)$ are in good agreement with the analytical calculations. This means that, in the scenario of a weak cavity driving, the analytical solutions derived from the Schrödinger equation approach in the steady state can well reproduce the full numerical solutions obtained by the master equation approach.

On the other hand, it can be easily seen from Figs. 3(a)–3(d) that the occurrence of the photon antibunching corresponds to the existence of the VIC effect (the red dotted lines). This means that the photon antibunching can be an important witness for the VIC effect and can be used to probe the existence of the VIC effect, which is different from the previous work in Ref. [4] that employs the VIQB effect to probe the existence of the VIC effect. The method that the photon antibunching can serve as a tool to probe the existence of the VIC effect can be used for investigating the energy transfer [104–106]. The construction of the bridge between the photon antibunching and the VIC effect has potential applications in quantum information processing and quantum optics [107,108].

Apart from that, it is worth mentioning that the intensity of the emitted light from the ONF-based cavity is proportional to $I_c = \langle \hat{S}_{\text{out}}^\dagger \hat{S}_{\text{out}} \rangle = \kappa_{e2} \langle \hat{a}^\dagger \hat{a} \rangle = \kappa_{e2} n$ (collected photons per second, i.e., the so-called source brightness [52]), where

the average intracavity photon number is expressed by $n = \langle \hat{a}^\dagger \hat{a} \rangle$. We also plot the intensity I_c of the ONF-based cavity emission light as a function of the driving detuning $\Delta_p/2\pi$ with VIC (red dotted lines) and without VIC (blue solid lines) in Figs. 3(i)–3(l), corresponding to the four different cases of $g/2\pi = 1.3$ MHz [see Fig. 3(i)], $g/2\pi = 2.9$ MHz [see Fig. 3(j)], $g/2\pi = 4.3$ MHz [see Fig. 3(k)], and $g/2\pi = 7.8$ MHz [see Fig. 3(l)]. By comparing Figs. 3(a)–3(d) and 3(i)–3(l), it is observed that the strong antibunching effect can be detected near the large brightness at the same time in the ONF CQED system. In this scenario, the ONF CQED system can be regarded as an effective single-photon source device, which provides a guiding significance for practical experimental design to a certain extent.

In all the analysis above, however, we have not yet taken into account the nonresonant case of the control field, namely, $\Delta/2\pi \neq 0$. In order to more clearly show the influence of the control detuning parameter on the photon statistics of the ONF CQED system, we plot the two-dimensional color-scale map of the normalized equal-time second-order intensity correlation function $g^{(2)}(0)$ as a function of the driving detuning $\Delta_p/2\pi$ as well as the control detuning $\Delta/2\pi$ with VIC in Fig. 4. It can be clearly seen from the figure that the photon antibunching can occur when the control laser frequency ω is near resonance with the excited frequency ω_{10} (i.e., $\Delta/2\pi \rightarrow 0$; the dark blue area). What is more, the antibunching effect of the system can be improved by increasing the cavity-atom coupling strength $g/2\pi$. By comparing Figs. 4(a) ($g/2\pi = 1.3$ MHz), 4(b) ($g/2\pi = 2.9$ MHz), 4(c) ($g/2\pi = 4.3$ MHz), and 4(d) ($g/2\pi = 7.8$ MHz), the dark blue area of $g^{(2)}(0)$ broadens with the increase of the cavity-atom coupling strength $g/2\pi$. As compared to the previous scheme [103] of generating strong photon antibunching at near zero driving detuning in a three-level system, the strong photon antibunching can be achieved in a broad parameter region of the driving detuning in our scheme. This widened dark blue area of $g^{(2)}(0)$ relaxes the requirement for the driving frequency, which is conducive to achieving strong photon antibunching and realizing a tunable single-photon source.

To clearly show how the cavity-atom coupling strength $g/2\pi$ affects the antibunching effect of the system, we plot the normalized equal-time second-order intensity correlation function $g^{(2)}(0)$ as a function of the driving detuning $\Delta_p/2\pi$ for five different values of $g/2\pi$ with VIC in Fig. 5(a). As shown in Fig. 5(a), it can be observed that (i) the value of $g^{(2)}(0)$ increases with increasing the cavity-atom coupling strength $g/2\pi$ gradually near $\Delta_p/2\pi = 0$ and the degree of the photon antibunching decreases; (ii) when the driving detuning $\Delta_p/2\pi$ is large, for example, $\Delta_p/2\pi = 16$ MHz, the value of $g^{(2)}(0)$ rapidly decreases with increasing $g/2\pi$ gradually and the degree of the photon antibunching quickly increases; and (iii) a strong photon antibunching [$g^{(2)}(0) \simeq 0.003$] can occur at $\Delta_p/2\pi = 16$ MHz for $g/2\pi = 7.8$ MHz. When the driving detuning is near $\Delta_p/2\pi = 0$ MHz, a stronger photon antibunching effect [i.e., a smaller value of $g^{(2)}(0)$] corresponds to a smaller $g/2\pi$, which can relax the requirement for the cavity-atom coupling strength $g/2\pi$. Photon antibunching can occur in the weak-coupling regime [$g/2\pi = (1.3, 1.9, 2.9, 4.3)$ MHz], which is beneficial to the use of

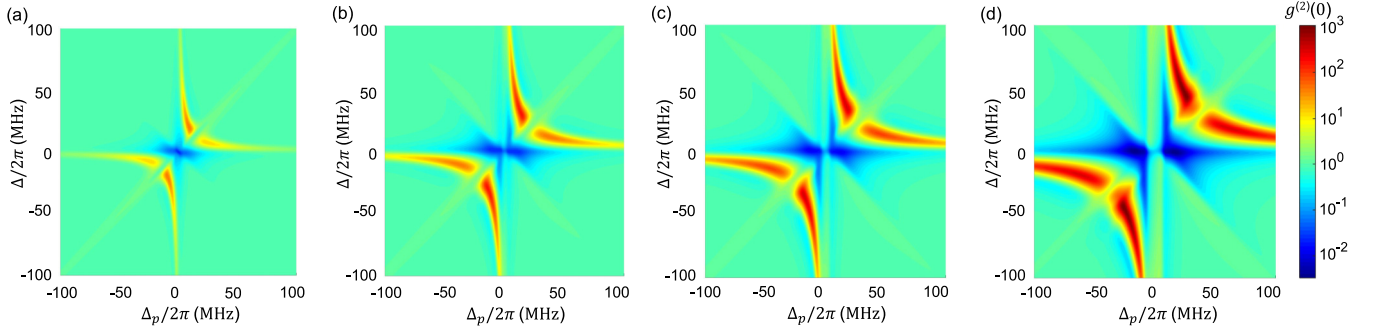


FIG. 4. Contour plot of the normalized equal-time second-order intensity correlation function $g^{(2)}(0)$ as a function of the driving detuning $\Delta_p/2\pi$ as well as the control detuning $\Delta/2\pi$ with VIC, corresponding to the four different cases of (a) $g/2\pi = 1.3$ MHz, (b) $g/2\pi = 2.9$ MHz, (c) $g/2\pi = 4.3$ MHz, and (d) $g/2\pi = 7.8$ MHz. The color bar on the right-hand side represents the magnitude of $g^{(2)}(0)$ and panels (a)–(d) share the same color bar. The other parameters are chosen as $\kappa/2\pi = 6.4$ MHz, $\Gamma_{11}/2\pi = 6.1$ MHz, $\Gamma_{22}/2\pi = 5/9 \times 6.1$ MHz, $\Gamma_{12}/2\pi = \sqrt{5/9} \times 6.1$ MHz, $\Omega/2\pi = 0.65$ MHz, $\eta/2\pi = 0.01$ MHz, and $\Delta_c/2\pi = 0$ MHz, respectively.

low-finesse cavities that are readily accessible in many CQED systems. Also, with the increase of the cavity-atom coupling strength ($g/2\pi = 7.8$ MHz), a smaller value of $g^{(2)}(0)$ can be achieved; i.e., the photon antibunching effect can become stronger.

To better illustrate the above-mentioned results presented in Fig. 5(a), we plot the normalized equal-time second-order intensity correlation function $g^{(2)}(0)$ as a function of the cavity-atom coupling strength $g/2\pi$ for the case of the driving detuning $\Delta_p/2\pi = 0$ MHz (the red dotted line and the purple circles) and $\Delta_p/2\pi = 16$ MHz (the blue solid line and the green triangles) with VIC in Fig. 5(b). It can be clearly seen

from Fig. 5(b) that when $\Delta_p/2\pi = 0$ MHz (the red dotted line and the purple circles), the value of $g^{(2)}(0)$ increases with increasing $g/2\pi$ gradually. When $\Delta_p/2\pi = 16$ MHz (the blue solid line and the green triangles), the value of $g^{(2)}(0)$ rapidly decreases with increasing $g/2\pi$ gradually, which is consistent with that shown in Fig. 5(a). In Fig. 5(b), the numerical results (the red dotted line and the blue solid line) of the normalized equal-time second-order intensity correlation function $g^{(2)}(0)$ obtained from the quantum master equation (3) are compared with the analytical results (the purple circles and the green triangles) given in Eqs. (22)–(25) from the Schrödinger equation in the steady-state limit, and they both are in good agreement.

Based on the numerical approach given by the quantum master equation (3), we now explore how the statistical property of the ONF CQED system is impacted by the cavity-atom coupling strength $g/2\pi$, the driving strength $\eta/2\pi$, and the control-field Rabi frequency $\Omega/2\pi$ by plotting the two-dimensional color-scale map of the normalized equal-time second-order intensity correlation function $g^{(2)}(0)$ in Fig. 6. It can be clearly seen from Fig. 6(a) that the strong photon antibunching (the dark blue area) can occur at a weak driving strength (near $\eta/2\pi = 0.01$ MHz) and a certain cavity-atom coupling strength (near $g/2\pi = 2.9$ MHz). In looking at the result of Fig. 6(b), we find that the strong photon antibunching (the dark blue area) can emerge at a weak driving strength (near $\eta/2\pi = 0.01$ MHz) and a certain control-field Rabi frequency (near $\Omega/2\pi = 0.65$ MHz). With the increase of the driving strength [i.e., $\eta \sim (g, \kappa)$], the photon bunching (the red, yellow, and green areas) can appear in the ONF CQED system, while the photon antibunching effect becomes weaker (the blue area becomes smaller and the blue becomes lighter). By tuning the driving strength $\eta/2\pi$, the conversion between the photon antibunching (the blue area) and the photon bunching (the red, yellow, and green areas) can be achieved in the ONF CQED system. From what has been analyzed above, we can reach the conclusion that the strong photon antibunching (the dark blue area) in the present ONF CQED system can be well generated by adjusting the cavity-atom coupling strength $g/2\pi$, the driving strength $\eta/2\pi$, and the control-field Rabi frequency $\Omega/2\pi$ appropriately.

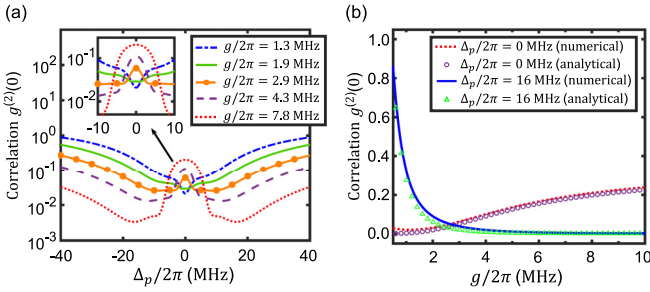


FIG. 5. (a) The normalized equal-time second-order intensity correlation function $g^{(2)}(0)$ as a function of the driving detuning $\Delta_p/2\pi$ for the five different values of the cavity-atom coupling strength $g/2\pi$ with VIC. The inset shows an enlarged view of $g^{(2)}(0)$ near $\Delta_p/2\pi = 0$. (b) The normalized equal-time second-order intensity correlation function $g^{(2)}(0)$ as a function of the cavity-atom coupling strength $g/2\pi$ for the case of the driving detuning $\Delta_p/2\pi = 0$ (the red dotted line and the purple circles) and $\Delta_p/2\pi = 16$ MHz (the blue solid line and the green triangles) with VIC. The panel uses the normal vertical axis to better display the fitting results. The red dotted line and the blue solid line correspond to the numerical results calculated by the quantum master equation (3). The purple circles and the green triangles correspond to the analytical results calculated by the closed-form expressions (22)–(25). The other parameters are chosen as $\kappa/2\pi = 6.4$ MHz, $\Gamma_{11}/2\pi = 6.1$ MHz, $\Gamma_{22}/2\pi = 5/9 \times 6.1$ MHz, $\Gamma_{12}/2\pi = \sqrt{5/9} \times 6.1$ MHz, $\Omega/2\pi = 0.65$ MHz, $\eta/2\pi = 0.01$ MHz, $\Delta/2\pi = 0$ MHz, and $\Delta_c/2\pi = 0$ MHz, respectively.

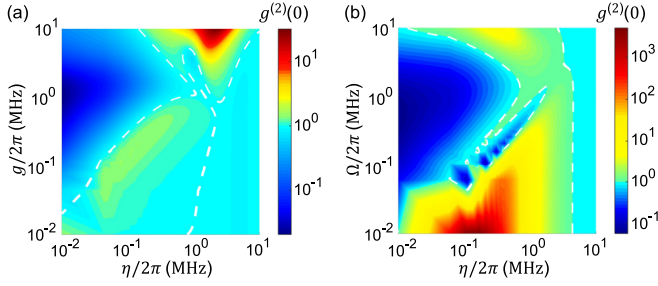


FIG. 6. (a) Contour plot of the normalized equal-time second-order intensity correlation function $g^{(2)}(0)$ as a function of the driving strength $\eta/2\pi$ as well as the cavity-atom coupling strength $g/2\pi$ for the control-field Rabi frequency $\Omega/2\pi = 0.65$ MHz with VIC. (b) Contour plot of the normalized equal-time second-order intensity correlation function $g^{(2)}(0)$ as a function of the driving strength $\eta/2\pi$ as well as the control-field Rabi frequency $\Omega/2\pi$ for the cavity-atom coupling strength $g/2\pi = 2.9$ MHz with VIC. The color bar on the right-hand side of panels (a) and (b) represents the magnitude of $g^{(2)}(0)$. The white contour lines in panels (a) and (b) correspond to $g^{(2)}(0) = 1$ (i.e., Poissonian light). The other parameters are chosen as $\kappa/2\pi = 6.4$ MHz, $\Gamma_{11}/2\pi = 6.1$ MHz, $\Gamma_{22}/2\pi = 5/9 \times 6.1$ MHz, $\Gamma_{12}/2\pi = \sqrt{5/9} \times 6.1$ MHz, $\Delta_p/2\pi = 0$ MHz, $\Delta/2\pi = 0$ MHz, and $\Delta_c/2\pi = 0$ MHz, respectively.

VI. CONCLUSIONS AND OUTLOOK

In summary, we have investigated the use of coherence statistics of photon antibunching to probe the existence of VIC and demonstrated that the VIQB can enable strong photon antibunching accompanying with large brightness in a coupled ONF CQED system. We find that the occurrence of the photon antibunching corresponds to the existence of VIC, indicating that the photon antibunching can be an important witness for VIC and can be used to probe the existence of VIC. By tuning the system parameters appropriately, a strong photon antibunching can occur in the weak-coupling “bad-cavity” regime when the VIQB is present, as a result of the destructive quantum interference between the different paths for two-photon excitation, which is beneficial to the use of low-finesse cavities that are readily accessible in many CQED systems. In this case, the strong photon antibunching can be detected near the strong intensity of the emitted light from the ONF-based cavity at the same time, which provides a guiding significance for practical experimental design to a certain extent. When the driving laser frequency is near resonance with the frequency of the cavity mode (i.e., the driving detuning is near zero), the degree of the photon antibunching increases with the decrease of the cavity-atom coupling strength, which can relax the requirement for the cavity-atom coupling strength in the ONF CQED system. Furthermore, we find that when the control detuning is near zero, the driving frequency range for achieving strong antibunching can be extended with the increase of the cavity-atom coupling strength, which can relax the requirement for the driving frequency in the ONF CQED system. This tunable atom-cavity scheme provides a possibility for the generation of a tunable single-photon source. In addition, we compare the analytical solutions of the second-order intensity correlation function obtained from the closed-form formulas with the numerical solutions obtained from the master

equation, and they are in good agreement. Also, we comment on a possible experimental implementation of our proposal with existing state-of-the-art ONF CQED architecture. We hope that the achievable results in our work can be useful for building a tunable single-photon source and enabling potential applications in quantum information processing [57,58] and quantum communications [59,60].

As a direct extension, it would be interesting to study the generation of telecom-band photons [e.g., O-band (1260–1360 nm) and C-band (1530–1565 nm)] in optical fibers due to their compatibility with existing fiber-optic infrastructure and the potential for minimal loss in fiber networks [109–112]. According to the previous works [113,114], it may be possible to replace Rb atom corresponding to 780 nm photon emission with Er^{3+} ion corresponding to 1532 nm or 1536.46 nm photon emission (C-band). Besides this, adopting the techniques introduced in Ref. [115], one can replace the Rb atom corresponding to 780 nm photon emission with a Ca^+ ion corresponding to 866 nm photon emission which is then converted to 1530 nm photon emission (C-band), while preserving their quantum statistics. As shown in Ref. [116], by demonstrating ion-photon entanglement, it may also be feasible to utilize 1310 nm photons (O-band) instead of 780 nm photons. In our ONF CQED system, the extension of 780 nm photons to low-loss telecom-band photons is left for further study. Finally, it is worth pointing out that, compared to another scheme [117] for implementing a 780 nm single-photon source using resonant driving frequency, in our scheme the strong photon antibunching can be achieved, on the one hand, in a broad parameter region of the driving frequency, which relaxes the requirement for the driving frequency, and on the other hand, in the bad-cavity regime, which is much easier to achieve, experimentally.

ACKNOWLEDGMENTS

We are grateful to Xin-You Lü and Rong Yu for stimulating discussions. The present research is supported partially by the National Natural Science Foundation of China (NSFC) through Grant No. 12275092 and by the National Key Research and Development Program of China under Contract No. 2021YFA1400700.

APPENDIX: CALCULATIONS FOR THE BEAT DYNAMICS

In this Appendix, we present the derivation of the atomic population σ_{22} [see Figs. 3(e)–3(h)] using a perturbation method [118] which is omitted in the main text. Based on the formula $\partial\langle\hat{O}\rangle/\partial t = \text{Tr}[\partial(\hat{O}\hat{\rho})/\partial t] = \text{Tr}[\hat{O}\partial\hat{\rho}/\partial t]$ [119] and the Lindblad master equation (3), one can derive the Heisenberg-Langevin equation of motion for the expectation value of any operator \hat{O} [118], with the form

$$\begin{aligned} \frac{\partial\langle\hat{O}\rangle}{\partial t} = & \text{Tr}\{-i[\hat{O}, \hat{H}_{\text{rot}}]\hat{\rho} + \hat{O}[\kappa\mathcal{D}(a)\hat{\rho} \\ & + \Gamma_{11}\mathcal{D}(\hat{\sigma}_{01})\hat{\rho} + \Gamma_{22}\mathcal{D}(\hat{\sigma}_{02})\hat{\rho} \\ & + \Gamma_{12}(\hat{\sigma}_{01}\hat{\rho}\hat{\sigma}_{02}^\dagger - \hat{\sigma}_{02}^\dagger\hat{\sigma}_{01}\hat{\rho}/2 - \hat{\rho}\hat{\sigma}_{02}^\dagger\hat{\sigma}_{01}/2) \\ & + \Gamma_{12}(\hat{\sigma}_{02}\hat{\rho}\hat{\sigma}_{01}^\dagger - \hat{\sigma}_{01}^\dagger\hat{\sigma}_{02}\hat{\rho}/2 - \hat{\rho}\hat{\sigma}_{01}^\dagger\hat{\sigma}_{02}/2)]\}, \end{aligned} \quad (\text{A1})$$

where \hat{H}_{rot} corresponds to the effective Hamiltonian directly yielded by Eq. (2) of the main text and $\langle \cdot \rangle$ stands for the expectation value. In accordance with the previous reports in Refs. [118, 120, 121], we can ignore the entanglement between the atom and the ONF cavity field. For the sake of brevity in notations, we can define $\sigma_{lm} = \langle \hat{\sigma}_{lm} \rangle$ ($l, m = 0, 1, 2$) and $a = \langle \hat{a} \rangle$ in the weak-driving limit. Using the cyclic permutation of the trace [$\text{Tr}(\hat{O}\hat{Q}) = \text{Tr}(\hat{Q}\hat{O})$], we finally can arrive at the following Heisenberg-Langevin equations of motion for the expectation values of σ_{lm} ($l, m = 0, 1, 2$) and a , which are given by

$$\begin{aligned} \dot{\sigma}_{00} = & \Gamma_{11}\sigma_{11} + \Gamma_{22}\sigma_{22} + \Gamma_{12}(\sigma_{12} + \sigma_{21}) - iga^*\sigma_{02} \\ & + iga\sigma_{20} - i\Omega\sigma_{01} + i\Omega\sigma_{10}, \end{aligned} \quad (\text{A2})$$

$$\dot{\sigma}_{11} = -\Gamma_{11}\sigma_{11} - \Gamma_{12}(\sigma_{12} + \sigma_{21})/2 + i\Omega\sigma_{01} - i\Omega\sigma_{10}, \quad (\text{A3})$$

$$\dot{\sigma}_{22} = -\Gamma_{22}\sigma_{22} - \Gamma_{12}(\sigma_{12} + \sigma_{21})/2 + iga^*\sigma_{02} - iga\sigma_{20}, \quad (\text{A4})$$

$$\begin{aligned} \dot{\sigma}_{01} = & -(i\Delta + \Gamma_{11}/2)\sigma_{01} - \Gamma_{12}\sigma_{02}/2 + iga\sigma_{21} \\ & + i\Omega(\sigma_{11} - \sigma_{00}), \end{aligned} \quad (\text{A5})$$

$$\begin{aligned} \dot{\sigma}_{02} = & -[i(\Delta_p + \Delta_c) + \Gamma_{22}/2]\sigma_{02} - \Gamma_{12}\sigma_{01}/2 \\ & + iga(\sigma_{22} - \sigma_{00}) + i\Omega\sigma_{12}, \end{aligned} \quad (\text{A6})$$

$$\begin{aligned} \dot{\sigma}_{21} = & -[i(\Delta - \Delta_p - \Delta_c) + \Gamma_{11}/2 + \Gamma_{22}/2]\sigma_{21} \\ & - \Gamma_{12}(\sigma_{11} + \sigma_{22})/2 + iga^*\sigma_{01} - i\Omega\sigma_{20}, \end{aligned} \quad (\text{A7})$$

$$\dot{a} = -(i\Delta_p + \kappa/2)a - ig\sigma_{02} + \eta, \quad (\text{A8})$$

where Γ_{11} and Γ_{22} are respectively the damping rates of the excited states $|1\rangle$ and $|2\rangle$ to the ground state $|0\rangle$, which are associated with the terms $\pm\Gamma_{11}\sigma_{11}$ and $\pm\Gamma_{22}\sigma_{22}$ in Eqs. (A2)–(A4). Γ_{12} represents the cross-damping rate between the excited states $|1\rangle$ and $|2\rangle$ (i.e., the VIC), which is associated with the terms $\Gamma_{12}(\sigma_{12} + \sigma_{21})$ and $-\Gamma_{12}(\sigma_{12} + \sigma_{21})/2$ in Eqs. (A2)–(A4). This set of ordinary nonlinear differential coupled equations describes the time evolution of the coupled ONF CQED system. Above, the overdots represent the derivatives with respect to time t .

In accordance with the previous experimental report in Ref. [4], we can assume that the atomic populations in the initial state are $\sigma_{22} \approx 0$, $\sigma_{11} \approx 10^{-10}$, and $\sigma_{00} \approx 1$, and the absolute values of the coherences are $|\sigma_{12}| \approx 0$, $|\sigma_{10}| \approx 10^{-5}$, and $|\sigma_{20}| \approx 0$. The average photon number can be assumed to $|a|^2 \approx 0$ at the initial time. By recurrently solving Eqs. (A2)–(A8), without the need for making the truncation approximation like the Schrödinger equation approach [i.e., Eq. (6)], we can well acquire the atomic population σ_{22} [see Figs. 3(e)–3(h)] as a function of time t .

-
- [1] E. T. Jaynes, in *Foundations of Radiation Theory and Quantum Electrodynamics*, edited by A. O. Barut (Springer, New York, 1980).
- [2] A. Lee, H. S. Han, F. K. Fatemi, S. L. Rolston, and K. Sinha, Collective quantum beats from distant multilevel emitters, *Phys. Rev. A* **107**, 013701 (2023).
- [3] H. M. Castro-Beltrán, O. de los Santos-Sánchez, L. Gutiérrez, and A. D. Alcantar-Vidal, Quantum interference in the resonance fluorescence of a $J = 1/2 - J' = 1/2$ atomic system: Quantum beats, nonclassicality, and non-Gaussianity, [arXiv:2301.03061](https://arxiv.org/abs/2301.03061).
- [4] H. S. Han, A. Lee, K. Sinha, F. K. Fatemi, and S. L. Rolston, Observation of Vacuum-Induced Collective Quantum Beats, *Phys. Rev. Lett.* **127**, 073604 (2021), see also accompanying online supplemental material.
- [5] V. Langer, H. Stolz, and W. von der Osten, Observation of Quantum Beats in the Resonance Fluorescence of Free Excitons, *Phys. Rev. Lett.* **64**, 854 (1990).
- [6] Z. Ficek and B. C. Sanders, Quantum beats in two-atom resonance fluorescence, *Phys. Rev. A* **41**, 359 (1990).
- [7] E. O. Göbel, K. Leo, T. C. Damen, J. Shah, S. Schmitt-Rink, W. Schäfer, J. F. Müller, and K. Köhler, Quantum Beats of Excitons in Quantum Wells, *Phys. Rev. Lett.* **64**, 1801 (1990).
- [8] K.-H. Pantke, D. Oberhauser, V. G. Lyssenko, J. M. Hvam, and G. Weimann, Coherent generation and interference of excitons and biexcitons in GaAs/Al_xGa_{1-x}As quantum wells, *Phys. Rev. B* **47**, 2413 (1993).
- [9] S. Bar-Ad and I. Bar-Joseph, Absorption Quantum Beats of Magnetoexcitons in GaAs Heterostructures, *Phys. Rev. Lett.* **66**, 2491 (1991).
- [10] P. Palinginis and H. Wang, Vanishing and Emerging of Absorption Quantum Beats from Electron Spin Coherence in GaAs Quantum Wells, *Phys. Rev. Lett.* **92**, 037402 (2004).
- [11] K. Leo, T. C. Damen, J. Shah, and K. Köhler, Quantum beats of free and bound excitons in GaAs/Al_xGa_{1-x}As quantum wells, *Phys. Rev. B* **42**, 11359 (1990).
- [12] S. Haroche, J. A. Paisner, and A. L. Schawlow, Hyperfine Quantum Beats Observed in Cs Vapor under Pulsed Dye Laser Excitation, *Phys. Rev. Lett.* **30**, 948 (1973).
- [13] C. G. Wade, N. Šibalić, J. Keaveney, C. S. Adams, and K. J. Weatherill, Probing an excited-state atomic transition using hyperfine quantum-beat spectroscopy, *Phys. Rev. A* **90**, 033424 (2014).
- [14] E. Hack and J. R. Huber, Quantum beat spectroscopy of molecules, *Int. Rev. Phys. Chem.* **10**, 287 (1991).
- [15] M. Winter, R. Schmidt, and U. Thumm, Multidimensional quantum-beat spectroscopy: Towards the complete temporal and spatial resolution of the nuclear dynamics in small molecules, *Phys. Rev. A* **80**, 031401(R) (2009).
- [16] I. E. Kozin, V. G. Davydov, I. V. Ignatiev, A. V. Kavokin, K. V. Kavokin, G. Malpuech, H.-W. Ren, M. Sugisaki, S. Sugou, and Y. Masumoto, Zero-field spin quantum beats in charged quantum dots, *Phys. Rev. B* **65**, 241312(R) (2002).
- [17] J. Bylsma, P. Dey, J. Paul, S. Hoogland, E. H. Sargent, J. M. Luther, M. C. Beard, and D. Karaiskaj, Quantum beats due to excitonic ground-state splitting in colloidal quantum dots, *Phys. Rev. B* **86**, 125322 (2012).
- [18] H. Stolz, V. Langer, E. Schreiber, S. Permogorov, and W. von der Osten, Picosecond Quantum-Beat Spectroscopy of Bound Excitons in CdS, *Phys. Rev. Lett.* **67**, 679 (1991).

- [19] T. Flissikowski, A. Hundt, M. Lowisch, M. Rabe, and F. Henneberger, Photon Beats from a Single Semiconductor Quantum Dot, *Phys. Rev. Lett.* **86**, 3172 (2001).
- [20] X. Yang, C. Vaswani, C. Sundahl, M. Mootz, L. Luo, J. H. Kang, I. E. Perakis, C. B. Eom, and J. Wang, Lightwave-driven gapless superconductivity and forbidden quantum beats by terahertz symmetry breaking, *Nat. Photonics* **13**, 707 (2019).
- [21] T. Chanelière, D. N. Matsukevich, S. D. Jenkins, T. A. B. Kennedy, M. S. Chapman, and A. Kuzmich, Quantum Telecommunication Based on Atomic Cascade Transitions, *Phys. Rev. Lett.* **96**, 093604 (2006).
- [22] W.-T. Liao, A. Pálffy, and C. H. Keitel, Coherent Storage and Phase Modulation of Single Hard-X-Ray Photons Using Nuclear Excitons, *Phys. Rev. Lett.* **109**, 197403 (2012).
- [23] X. Li, Y. Wu, D. G. Steel, D. Gammon, and L. J. Sham, Raman coherence beats from the entangled state involving polarized excitons in single quantum dots, *Phys. Rev. B* **70**, 195330 (2004).
- [24] H. Goto, H. Katsuki, H. Ibrahim, H. Chiba, and K. Ohmori, Strong-laser-induced quantum interference, *Nat. Phys.* **7**, 383 (2011).
- [25] D. G. Norris, L. A. Orozco, P. Barberis-Blostein, and H. J. Carmichael, Observation of Ground-State Quantum Beats in Atomic Spontaneous Emission, *Phys. Rev. Lett.* **105**, 123602 (2010).
- [26] G.-Z. Song, E. Munro, W. Nie, F.-G. Deng, G.-J. Yang, and L.-C. Kwek, Photon scattering by an atomic ensemble coupled to a one-dimensional nanophotonic waveguide, *Phys. Rev. A* **96**, 043872 (2017).
- [27] A. Pal and B. Deb, Photon-photon correlations with a V-type three-level system interacting with two quantized field modes, *Opt. Commun.* **431**, 1 (2019).
- [28] A. Imamoğlu, H. Schmidt, G. Woods, and M. Deutsch, Strongly Interacting Photons in a Nonlinear Cavity, *Phys. Rev. Lett.* **79**, 1467 (1997).
- [29] H. J. Kimble, in *Cavity Quantum Electrodynamics*, edited by P. Berman (Academic, San Diego, 1994).
- [30] H. Mabuchi and A. C. Doherty, Cavity quantum electrodynamics: Coherence in context, *Science* **298**, 1372 (2002).
- [31] J. M. Fink, M. Göppl, M. Baur, R. Bianchetti, P. J. Leek, A. Blais, and A. Wallraff, Climbing the Jaynes-Cummings ladder and observing its \sqrt{n} nonlinearity in a cavity QED system, *Nature (London)* **454**, 315 (2008).
- [32] B. W. Shore and P. L. Knight, The Jaynes-Cummings model, *J. Mod. Opt.* **40**, 1195 (1993).
- [33] J. Kasprzak, S. Reitzenstein, E. A. Muljarov, C. Kistner, C. Schneider, M. Strauss, S. Höling, A. Forchel, and W. Langbein, Up on the Jaynes-Cummings ladder of a quantum-dot/microcavity system, *Nat. Mater.* **9**, 304 (2010).
- [34] F. P. Laussy, E. del Valle, M. Schrapp, A. Laucht, and J. J. Finley, Climbing the Jaynes-Cummings ladder by photon counting, *J. Nanophotonics* **6**, 061803 (2012).
- [35] X. Liang, Z. Duan, Q. Guo, C. Liu, S. Guan, and Y. Ren, Antibunching effect of photons in a two-level emitter-cavity system, *Phys. Rev. A* **100**, 063834 (2019).
- [36] T. Shi, S. Fan, and C. P. Sun, Two-photon transport in a waveguide coupled to a cavity in a two-level system, *Phys. Rev. A* **84**, 063803 (2011).
- [37] E. V. Stolyarov, Few-photon Fock-state wave packet interacting with a cavity-atom system in a waveguide: Exact quantum state dynamics, *Phys. Rev. A* **99**, 023857 (2019).
- [38] Z. Li, X. Li, and X. Zhong, Strong photon blockade in an all-fiber emitter-cavity quantum electrodynamics system, *Phys. Rev. A* **103**, 043724 (2021).
- [39] H. J. Kimble, M. Dagenais, and L. Mandel, Photon Antibunching in Resonance Fluorescence, *Phys. Rev. Lett.* **39**, 691 (1977).
- [40] B. Dayan, A. S. Parkins, T. Aoki, E. P. Ostby, K. J. Vahala, and H. J. Kimble, A photon turnstile dynamically regulated by one atom, *Science* **319**, 1062 (2008).
- [41] A. Reinhard, T. Volz, M. Winger, A. Badolato, K. J. Hennessy, E. L. Hu, and A. Imamoğlu, Strongly correlated photons on a chip, *Nat. Photonics* **6**, 93 (2012).
- [42] T. C. H. Liew and V. Savona, Single Photons from Coupled Quantum Modes, *Phys. Rev. Lett.* **104**, 183601 (2010).
- [43] M. Bamba, A. Imamoğlu, I. Carusotto, and C. Ciuti, Origin of strong photon antibunching in weakly nonlinear photonic molecules, *Phys. Rev. A* **83**, 021802(R) (2011).
- [44] H. Flayac and V. Savona, Unconventional photon blockade, *Phys. Rev. A* **96**, 053810 (2017).
- [45] H. J. Sniijders, J. A. Frey, J. Norman, H. Flayac, V. Savona, A. C. Gossard, J. E. Bowers, M. P. van Exter, D. Bouwmeester, and W. Löffler, Observation of the Unconventional Photon Blockade, *Phys. Rev. Lett.* **121**, 043601 (2018).
- [46] B. Lounis and M. Orrit, Single-photon sources, *Rep. Prog. Phys.* **68**, 1129 (2005).
- [47] S. Buckley, K. Rivoire, and J. Vučković, Engineered quantum dot single-photon sources, *Rep. Prog. Phys.* **75**, 126503 (2012).
- [48] G.-C. Shan, Z.-Q. Yin, C. H. Shek, and W. Huang, Single photon sources with single semiconductor quantum dots, *Front. Phys.* **9**, 170 (2014).
- [49] P. Kok, W. J. Munro, K. Nemoto, T. C. Ralph, J. P. Dowling, and G. J. Milburn, Linear optical quantum computing with photonic qubits, *Rev. Mod. Phys.* **79**, 135 (2007).
- [50] A. Kuhn and D. Ljunggren, Cavity-based single-photon sources, *Contemp. Phys.* **51**, 289 (2010).
- [51] E. Togan, Y. Chu, A. S. Trifonov, L. Jiang, J. Maze, L. Childress, M. V. G. Dutt, A. S. Sørensen, P. R. Hemmer, A. S. Zibrov, and M. D. Lukin, Quantum entanglement between an optical photon and a solid-state spin qubit, *Nature (London)* **466**, 730 (2010).
- [52] P. Senellart, G. Solomon, and A. White, High-performance semiconductor quantum-dot single-photon sources, *Nat. Nanotechnol.* **12**, 1026 (2017).
- [53] R. Yalla, M. Sadgrove, K. P. Nayak, and K. Hakuta, Cavity Quantum Electrodynamics on a Nanofiber Using a Composite Photonic Crystal Cavity, *Phys. Rev. Lett.* **113**, 143601 (2014).
- [54] S. Kato and T. Aoki, Strong Coupling between a Trapped Single Atom and an All-Fiber Cavity, *Phys. Rev. Lett.* **115**, 093603 (2015).
- [55] K. P. Nayak, M. Sadgrove, R. Yalla, F. Le Kien, and K. Hakuta, Nanofiber quantum photonics, *J. Opt.* **20**, 073001 (2018).
- [56] K. P. Nayak, J. Wang, and J. Keloth, Real-Time Observation of Single Atoms Trapped and Interfaced to a Nanofiber Cavity, *Phys. Rev. Lett.* **123**, 213602 (2019).
- [57] A. Kiraz, M. Atatüre, and A. Imamoğlu, Quantum-dot single-photon sources: Prospects for applications in linear optics

- quantum-information processing, *Phys. Rev. A* **69**, 032305 (2004).
- [58] K. Stannigel, P. Komar, S. J. M. Habraken, S. D. Bennett, M. D. Lukin, P. Zoller, and P. Rabl, Optomechanical Quantum Information Processing with Photons and Phonons, *Phys. Rev. Lett.* **109**, 013603 (2012).
- [59] A. Kuhn, M. Hennrich, and G. Rempe, Deterministic Single-Photon Source for Distributed Quantum Networking, *Phys. Rev. Lett.* **89**, 067901 (2002).
- [60] L. Aolita and S. P. Walborn, Quantum Communication without Alignment using Multiple-Qubit Single-Photon States, *Phys. Rev. Lett.* **98**, 100501 (2007).
- [61] G. C. Hegerfeldt and M. B. Plenio, Quantum beats revisited: A quantum jump approach, *Quantum Opt.* **6**, 15 (1994).
- [62] K. Qu and G. S. Agarwal, Generating quadrature squeezed light with dissipative optomechanical coupling, *Phys. Rev. A* **91**, 063815 (2015).
- [63] J. Li, Y. Qu, R. Yu, and Y. Wu, Generation and control of optical frequency combs using cavity electromagnetically induced transparency, *Phys. Rev. A* **97**, 023826 (2018).
- [64] M. O. Scully and M. S. Zubairy, *Quantum Optics* (Cambridge University Press, Cambridge, UK, 1997).
- [65] P. Meystre and M. Sargent, *Elements of Quantum Optics* (Springer, Berlin, 2013).
- [66] H. J. Carmichael, *Statistical Methods in Quantum Optics 1: Master Equations and Fokker-Planck Equations* (Springer, New York, 1999).
- [67] G. S. Agarwal, *Quantum Optics* (Cambridge University Press, Cambridge, UK, 2013).
- [68] C. W. Gardiner and P. Zoller, *Quantum Noise* (Springer-Verlag, New York, 2005).
- [69] D. Walls and G. Milburn, *Quantum Optics* (Springer, Berlin, 1994).
- [70] R. Loudon, *The Quantum Theory of Light* (Oxford University, Oxford, UK, 2003).
- [71] K. M. Birnbaum, A. Boca, R. Miller, A. D. Boozer, T. E. Northup, and H. J. Kimble, Photon blockade in an optical cavity with one trapped atom, *Nature (London)* **436**, 87 (2005).
- [72] J. Li and Y. Wu, Quality of photon antibunching in two cavity-waveguide arrangements on a chip, *Phys. Rev. A* **98**, 053801 (2018).
- [73] J. C. Loredo, M. A. Broome, P. Hilaire, O. Gazzano, I. Sagnes, A. Lemaitre, M. P. Almeida, P. Senellart, and A. G. White, Boson Sampling with Single-Photon Fock States from a Bright Solid-State Source, *Phys. Rev. Lett.* **118**, 130503 (2017).
- [74] S. E. Thomas, M. Billard, N. Coste, S. C. Wein, Priya, H. Ollivier, O. Krebs, L. Tazaïrt, A. Harouri, A. Lemaitre, I. Sagnes, C. Anton, L. Lanco, N. Somaschi, J. C. Loredo, and P. Senellart, Bright Polarized Single-Photon Source Based on a Linear Dipole, *Phys. Rev. Lett.* **126**, 233601 (2021).
- [75] K. Seibold, R. Rota, and V. Savona, Dissipative time crystal in an asymmetric nonlinear photonic dimer, *Phys. Rev. A* **101**, 033839 (2020).
- [76] R. Rota and V. Savona, Simulating frustrated antiferromagnets with quadratically driven QED cavities, *Phys. Rev. A* **100**, 013838 (2019).
- [77] H. Flayac and V. Savona, Input-output theory of the unconventional photon blockade, *Phys. Rev. A* **88**, 033836 (2013).
- [78] H. J. Carmichael, *Statistical Methods in Quantum Optics 2: Nonclassical Fields* (Springer, Berlin, 2008).
- [79] R. Sáez-Blázquez, J. Feist, F. J. García-Vidal, and A. I. Fernández-Domínguez, Photon statistics in collective strong coupling: Nanocavities and microcavities, *Phys. Rev. A* **98**, 013839 (2018).
- [80] F. Minganti, A. Miranowicz, R. W. Chhajlany, and F. Nori, Quantum exceptional points of non-Hermitian Hamiltonians and Liouvillians: The effects of quantum jumps, *Phys. Rev. A* **100**, 062131 (2019).
- [81] Y. H. Zhou, H. Z. Shen, and X. X. Yi, Unconventional photon blockade with second-order nonlinearity, *Phys. Rev. A* **92**, 023838 (2015).
- [82] Y. Liu, G. Wang, Y. Liu, and F. Nori, Mode coupling and photon antibunching in a bimodal cavity containing a dipole quantum emitter, *Phys. Rev. A* **93**, 013856 (2016).
- [83] D. A. Steck, Rubidium 85 D line data, <http://steck.us/alkalidata> (revision 2.2.3, 9 July 2021).
- [84] M. Hennrich, A. Kuhn, and G. Rempe, Transition from Antibunching to Bunching in Cavity QED, *Phys. Rev. Lett.* **94**, 053604 (2005).
- [85] P. Zhou and S. Swain, Ultranarrow Spectral Lines via Quantum Interference, *Phys. Rev. Lett.* **77**, 3995 (1996).
- [86] E. Paspalakis, S. Gong, and P. L. Knight, Spontaneous emission-induced coherent effects in absorption and dispersion of a V-type three-level atom, *Opt. Commun.* **152**, 293 (1998).
- [87] S. Menon and G. S. Agarwal, Effects of spontaneously generated coherence on the pump-probe response of a Λ system, *Phys. Rev. A* **57**, 4014 (1998).
- [88] H. Ma, S. Gong, C. Liu, Z. Sun, and Z. Xu, Effects of spontaneous emission-induced coherence on population inversion in a ladder-type atomic system, *Opt. Commun.* **223**, 97 (2003).
- [89] C. Wang, Z. Kang, S. Tian, Y. Jiang, and J. Gao, Effect of spontaneously generated coherence on absorption in a V-type system: Investigation in dressed states, *Phys. Rev. A* **79**, 043810 (2009).
- [90] Y. Lien, G. Barontini, M. Scheucher, M. Mergenthaler, J. Goldwin, and E. A. Hinds, Observing coherence effects in an overdamped quantum system, *Nat. Commun.* **7**, 13933 (2016).
- [91] K. P. Nayak, F. Le Kien, Y. Kawai, K. Hakuta, K. Nakajima, H. T. Miyazaki, and Y. Sugimoto, Cavity formation on an optical nanofiber using focused ion beam milling technique, *Opt. Express* **19**, 14040 (2011).
- [92] F. Le Kien, K. P. Nayak, and K. Hakuta, Nanofibers with Bragg gratings from equidistant holes, *J. Mod. Opt.* **59**, 274 (2012).
- [93] K. P. Nayak and K. Hakuta, Photonic crystal formation on optical nanofibers using femtosecond laser ablation technique, *Opt. Express* **21**, 2480 (2013).
- [94] J. Keloth, K. P. Nayak, and K. Hakuta, Fabrication of a centimeter-long cavity on a nanofiber for cavity quantum electrodynamics, *Opt. Lett.* **42**, 1003 (2017).
- [95] E. Vetsch, D. Reitz, G. Sagué, R. Schmidt, S. T. Dawkins, and A. Rauschenbeutel, Optical Interface Created by Laser-Cooled Atoms Trapped in the Evanescent Field Surrounding an Optical Nanofiber, *Phys. Rev. Lett.* **104**, 203603 (2010).
- [96] A. Goban, K. S. Choi, D. J. Alton, D. Ding, C. Lacroûte, M. Pototschnig, T. Thiele, N. P. Stern, and H. J. Kimble, Demonstration of a State-Insensitive, Compensated Nanofiber Trap, *Phys. Rev. Lett.* **109**, 033603 (2012).
- [97] H. L. Sørensen, J.-B. Béguin, K. W. Kluge, I. Iakoupov, A. S. Sørensen, J. H. Müller, E. S. Polzik, and J. Appel, Coherent

- Backscattering of Light Off One-Dimensional Atomic Strings, *Phys. Rev. Lett.* **117**, 133604 (2016).
- [98] A. Goban, C.-L. Hung, J. D. Hood, S.-P. Yu, J. A. Muniz, O. Painter, and H. J. Kimble, Superradiance for Atoms Trapped along a Photonic Crystal Waveguide, *Phys. Rev. Lett.* **115**, 063601 (2015).
- [99] Y. Meng, C. Liedl, S. Pucher, A. Rauschenbeutel, and P. Schneeweiss, Imaging and Localizing Individual Atoms Interfaced with a Nanophotonic Waveguide, *Phys. Rev. Lett.* **125**, 053603 (2020).
- [100] F. Le Kien and K. Hakuta, Cavity-enhanced channeling of emission from an atom into a nanofiber, *Phys. Rev. A* **80**, 053826 (2009).
- [101] F. Le Kien and K. Hakuta, Triggered generation of single guided photons from a single atom in a nanofiber cavity, *Phys. Rev. A* **83**, 043801 (2011).
- [102] C. Wuttke, M. Becker, S. Brückner, M. Rothhardt, and A. Rauschenbeutel, Nanofiber Fabry-Perot microresonator for nonlinear optics and cavity quantum electrodynamics, *Opt. Lett.* **37**, 1949 (2012).
- [103] J. Li, C. Ding, and Y. Wu, Enhanced photon antibunching via interference effects in a Δ configuration, *Phys. Rev. A* **100**, 033814 (2019).
- [104] G. S. Agarwal and A. K. Patnaik, Vacuum-induced coherences in radiatively coupled multilevel systems, *Phys. Rev. A* **63**, 043805 (2001).
- [105] J. Evers, M. Kiffner, M. Macovei, and C. H. Keitel, Geometry-dependent dynamics of two Λ -type atoms via vacuum-induced coherences, *Phys. Rev. A* **73**, 023804 (2006).
- [106] S. I. Schmid and J. Evers, Interplay of vacuum-mediated inter- and intra-atomic couplings in a pair of atoms, *Phys. Rev. A* **81**, 063805 (2010).
- [107] M. O. Scully, S.-Y. Zhu, and A. Gavrielides, Degenerate Quantum-Beat Laser: Lasing Without Inversion and Inversion Without Lasing, *Phys. Rev. Lett.* **62**, 2813 (1989).
- [108] S.-Y. Zhu and M. O. Scully, Spectral Line Elimination and Spontaneous Emission Cancellation via Quantum Interference, *Phys. Rev. Lett.* **76**, 388 (1996).
- [109] X. Cao, M. Zopf, and F. Ding, Telecom wavelength single photon sources, *J. Semicond.* **40**, 071901 (2019).
- [110] J. Yang, C. Nawrath, R. Keil, R. Joos, X. Zhang, B. Höfer, Y. Chen, M. Zopf, M. Jetter, S. L. Portalupi, F. Ding, P. Michler, and O. G. Schmidt, Quantum dot-based broadband optical antenna for efficient extraction of single photons in the telecom O-band, *Opt. Express* **28**, 19457 (2020).
- [111] J. D. Siverns, J. Hannegan, and Q. Quraishi, Neutral-Atom Wavelength-Compatible 780 nm Single Photons from a Trapped Ion via Quantum Frequency Conversion, *Phys. Rev. Appl.* **11**, 014044 (2019).
- [112] C. Chen, C. Xu, A. Riazi, E. Y. Zhu, A. C. B. Greenwood, A. V. Gladyshev, P. G. Kazansky, B. T. Kirby, and L. Qian, Telecom-band hyperentangled photon pairs from a fiber-based source, *Phys. Rev. A* **105**, 043702 (2022).
- [113] J. Jin, E. Saglamyurek, M. I. G. Puigibert, V. Verma, F. Marsili, S. W. Nam, D. Oblak, and W. Tittel, Telecom-Wavelength Atomic Quantum Memory in Optical Fiber for Heralded Polarization Qubits, *Phys. Rev. Lett.* **115**, 140501 (2015).
- [114] A. M. Dibos, M. Raha, C. M. Phenicie, and J. D. Thompson, Atomic Source of Single Photons in the Telecom Band, *Phys. Rev. Lett.* **120**, 243601 (2018).
- [115] T. Walker, K. Miyaniishi, R. Ikuta, H. Takahashi, S. V. Kashanian, Y. Tsujimoto, K. Hayasaka, T. Yamamoto, N. Imoto, and M. Keller, Long-Distance Single Photon Transmission from a Trapped Ion via Quantum Frequency Conversion, *Phys. Rev. Lett.* **120**, 203601 (2018).
- [116] M. Bock, P. Eich, S. Kucera, M. Kreis, A. Lenhard, C. Becher, and J. Eschner, High-fidelity entanglement between a trapped ion and a telecom photon via quantum frequency conversion, *Nat. Commun.* **9**, 1998 (2018).
- [117] L. Béguin, J. Jahn, J. Wolters, M. Reindl, Y. Huo, R. Trotta, A. Rastelli, F. Ding, O. G. Schmidt, P. Treutlein, and R. J. Warburton, On-demand semiconductor source of 780-nm single photons with controlled temporal wave packets, *Phys. Rev. B* **97**, 205304 (2018).
- [118] J. Li, S. Shen, C. Ding, and Y. Wu, Magnetically induced optical transparency in a plasmon-exciton system, *Phys. Rev. A* **103**, 053706 (2021).
- [119] H. Hapuarachchi, M. Premaratne, Q. Bao, W. Cheng, S. D. Gunapala, and G. P. Agrawal, Cavity QED analysis of an exciton-plasmon hybrid molecule via the generalized nonlocal optical response method, *Phys. Rev. B* **95**, 245419 (2017).
- [120] E. Waks and D. Sridharan, Cavity QED treatment of interactions between a metal nanoparticle and a dipole emitter, *Phys. Rev. A* **82**, 043845 (2010).
- [121] L. Wang, K. Di, Y. Zhu, and G. S. Agarwal, Interference control of perfect photon absorption in cavity quantum electrodynamics, *Phys. Rev. A* **95**, 013841 (2017).